JEM Journal of Experimental Medicine

ARTICLE

Zbtb32 promotes CD8⁺ T cell differentiation and function in cancer

Birui Pan[1], Qinli Sun[1], Ruifeng Li[1], Juan Feng[1], Jing Hao[2], Bowen Xie[1], Xiaohong Zhao[1], Zixuan Zhao[1], Peng Wei[1], Qiuyan Lan[3], Shiyuan Xie[1], Tian Xie[1], Yongzhen Chen[1], Kun Wei[1], Xuan Zhong[1], Hai Qi[1], Ling Ni[1], and Chen Dong[3]

In the tumor microenvironment (TME), "exhausted" CD8⁺ T cells are classified into progenitor (T_{pex}) and terminally exhausted (T_{tex}) populations. T_{pex} cells, critically regulated by zinc finger and BTB domain containing 27 (Zbtb27)/Bcl6 transcription factor, could be reinvigorated during immune checkpoint blockade (ICB) therapy, while T_{tex} cells, characterized by stronger proliferation and cytotoxicity, play an indispensable role in tumor control. However, the mechanisms governing the differentiation into T_{tex} and their function remain not well understood. In this study, we identified that Zbtb32, highly expressed in CD8⁺ T_{tex} subset, is crucial for CD8⁺ T cells within tumors. Zbtb32, regulated by CD28 signaling, promotes the differentiation of CD8⁺ T cells into T_{tex} subset, enhancing their cytotoxicity, proliferation, and anti-tumor capability. Importantly, we found a competitive DNA binding between Zbtb32 and Bcl6, especially in regulation of *Id2* expression. Thus, our findings demonstrate the pivotal role of Zbtb32 in CD8⁺ T cell anti-tumor function, with implications in cancer immunotherapy.

Introduction

CD8⁺ T cell exhaustion is a state of dysfunction that develops in response to persistent antigen exposure, particularly observed in chronic infection and cancer. The functional consequences of CD8⁺ T cell exhaustion are profound, severely limiting their ability to control tumors. CD8⁺ exhausted T (T_{ex}) cells are transcriptionally and epigenetically distinct from effector CD8⁺ T cells, featured by dampened effector and cytokine gene expression (Chen et al., 2019b; Gebhardt et al., 2023). Continuous presence of tumor antigens in the immunosuppressive tumor microenvironment (TME) results in T cell exhaustion (Wherry and Kurachi, 2015; Philip and Schietinger, 2022; Dolina et al., 2021; McLane et al., 2019), marked by the upregulation of inhibitory receptors such as PD-1 and CTLA-4 (Ribas and Wolchok, 2018).

Within CD8⁺ T_{ex} cell population, there exists a spectrum of differentiation states ranging from progenitor exhausted (T_{pex}) cells to terminally exhausted (T_{tex}) cells. CD8⁺ T_{pex} cells are an early subset in the exhaustion differentiation hierarchy (Gebhardt et al., 2023). These cells retain the potentials for proliferation and self-renewal, characterized by the expression of transcription factors (TFs) such as TCF1 and Bcl6 (Chen et al., 2019b; Utzschneider et al., 2016; Sun et al., 2023a; Wu et al., 2016). CD8⁺ T_{pex} cells respond to therapeutic interventions such as immune checkpoint blockade (ICB) (Miller et al., 2019; Utzschneider et al., 2016; Im et al., 2016; Kurtulus et al., 2019). In response to antigenic stimulation and perhaps the microenvironment, they progressively differentiate into T_{tex} cells, which are marked by strengthened cytolytic function but a gradual loss of proliferative capacity, making them less responsive to therapeutic interventions (Schietinger and Greenberg, 2014; Kurtulus et al., 2019; Paley et al., 2012). T_{tex} cells express high levels of multiple inhibitory receptors, including PD-1, TIM-3, and LAG-3 (Im et al., 2016; McLane et al., 2019; Andrews et al., 2017; Das et al., 2017). Increasing T_{pex} cell subpopulation and promoting their differentiation into T_{tex} cells has become an attractive strategy to enhance the long-term tumor control ability of CD8⁺ T cells. Therefore, researchers have attempted to identify key fate-determining factors that regulate CD8⁺ T cell stemness and differentiation in TME. For instance, TCF1 and TOX are crucial for T_{pex} cells (Chen et al., 2019b; Utzschneider et al., 2016; Seo et al., 2019; Niu and Wang, 2023; Scott et al., 2019; Yang et al., 2021; Khan et al., 2019; Kim et al., 2020), while Id2 and Blimp1 are essential for the induction and persistence of T_{tex} cells (Lagumdzic et al., 2022; Cannarile et al., 2006; Li et al., 2024; Yang et al., 2011; Omilusik et al., 2018; Sun et al., 2023a; Jung et al., 2022; Shin et al., 2009; Crotty et al., 2010). However, the molecular mechanisms underlying the differentiation of T_{pex} to T_{tex} cells are not well understood. Particularly, the

[1]Institute for Immunology, Tsinghua University, Beijing, China; [2]Shanghai Immune Therapy Institute, Shanghai Jiao Tong University School of Medicine-Affiliated Renji Hospital, Shanghai, China; [3]Westlake University School of Medicine, Hangzhou, China.

Correspondence to Chen Dong: dongchen@westlake.edu.cn.

maintenance of T_{tex} cells with potent cytotoxicity in TME still remains elusive.

Zinc finger and BTB domain containing (Zbtb) family TFs contain the BTB domain, which recruits cofactors and histone modification enzymes to the site of regulation, and the zinc finger domain, responsible for sequence-specific DNA binding (Kelly and Daniel, 2006; Beaulieu and Sant'Angelo, 2011; Cheng et al., 2021). Most Zbtb family members, such as PLZF (Zbtb16) and Bcl6 (Zbtb27), are critical in regulation of immune cells as classic transcriptional repressors (Hoatlin et al., 1999; Hatzi et al., 2015; Mondal et al., 2010). Our recent work has demonstrated a critical function of Bcl6 in $CD8^+$ tumor-infiltrated T cells (TILs), including the maintenance of T_{pex} cells, and repression of T_{tex} cell–associated gene expression, thus offering long-term tumor control (Sun et al., 2023a). Interestingly, Bcl6 functions to antagonize the expression and function of Blimp1, which is regulated by IL-2 signaling. Zbtb32, another member in the Zbtb family, has been reported to play important roles in different types of immune cells, including inhibition of $CD4^+$ T cell proliferation (Piazza et al., 2004), suppression of IL-4 gene activation (Omori et al., 2003), and restriction of memory B cell responses (Jash et al., 2016; Yoon et al., 2012), while positively regulating natural killer (NK) cell responses to infection (Beaulieu et al., 2014; Adams et al., 2018). During LCMV infection, *Zbtb32* expression was mainly observed in terminal effector $CD8^+$ T cells, rather than in naïve or memory subsets (Hudson et al., 2019), while *Zbtb32*-deficient $CD8^+$ T cells were shown to have enhanced antiviral response (Shin et al., 2017).

In this study, we identified Zbtb32 as an important TF in T_{tex} TILs, which promotes $CD8^+$ T cell effector function in tumor rejection. Interestingly, we discovered a competitive relationship of Zbtb32 and Bcl6 in tumor-specific $CD8^+$ T cell fate determination, providing valuable insights into future immunotherapeutic development.

Results

Zbtb32 is selectively expressed in T_{tex} $CD8^+$ TILs

To understand the fate determination of $CD8^+$ T cells in cancer, we investigated into differentially expressed TFs between T_{pex} and T_{tex} $CD8^+$ T cell subpopulations, marked by Bcl6 and Tim3 in E.G7 tumor-bearing mice (Sun et al., 2023a). Several well-known TFs, including *Prdm1* and *Id2*, were highly expressed in T_{tex} subset, whereas *Id3* and *Tcf7* were in T_{pex} subset (Fig. 1, A and B). Interestingly, we noted that *Zbtb32* exhibited upregulated expression levels in T_{tex} cells, as compared with T_{pex} cells.

Furthermore, by analyzing RNA-sequencing (RNA-seq) data from various human cancer types in TCGA datasets, we observed significant positive correlations between *ZBTB32* expression and that of T_{tex} signature gene (*CD8A*, *GZMB*, *GZMK*, *HAVCR2*, *ID2*, *IL2RA*, *IL2RB*, *LAG3*, *PDCD1*, *PRDM1*, and *TIGIT*) in different cancer models, among which skin cutaneous melanoma (SKCM) exhibited highest correlation (Fig. S1, A and B), suggesting that *ZBTB32* expression was increased with terminal differentiation of $CD8^+$ TILs. Specifically, upon dividing various cancer patients into subgroups with increased or decreased expression of T_{tex} signature genes, we found that *ZBTB32* expression exhibited significant increase in the subgroup enriched in expression of these genes, compared with that with decreased expression (Fig. S1, C and D).

To further elucidate the expression of *ZBTB32* in $CD8^+$ T cells from human cancer, we analyzed single-cell RNA-seq (scRNA-seq) data from melanoma patient samples (Fig. S1 E). Using *TCF7* and *HAVCR2* to distinguish $CD8^+$ TILs into two main populations, $CD8^+$ T_{pex} and T_{tex}, our results revealed a profound overlapping distribution of *ZBTB32* with *HAVCR2* and *GZMB* mRNAs (Fig. S1 F), indicating T_{tex} properties. Importantly, no overlap in mRNA expression was observed between *ZBTB32* and *TCF7* in cell subpopulations. Also, analysis of gene expression across distinct clusters revealed that *ZBTB32*, *HAVCR2*, and *GZMB* were predominantly expressed by T cells in clusters 0 and 4, whereas *TCF1* expression was exclusively concentrated in clusters 1, 2, and 3 (Fig. S1 G). This underscores the selective expression of *ZBTB32* in the T_{tex} subset rather than the T_{pex} subset of $CD8^+$ TILs.

Moreover, to further elucidate the pivotal role of ZBTB32 in $CD8^+$ T cell–mediated anti-tumor function, we analyzed clinical data from SKCM patients in TCGA, sorting them based on *CD8A* expression levels and getting two main groups from top 25% (CD8 enriched) and bottom 25% (CD8 decreased) of all. In this comparison, we only observed distinct survival rates between subgroups with high and low *ZBTB32* expression levels only within the $CD8^+$ T cell–enriched group, highlighting the potential benefits in patients with *ZBTB32*-expressing $CD8^+$ TILs (Fig. S1 H).

Additionally, we examined the published scRNA-seq dataset from murine B16-OVA tumor model (Miller et al., 2019), which consistently demonstrated substantial expression of *Zbtb32* in $CD8^+$ TILs; *Zbtb32* expression was mainly enriched in $CD8^+$ T cells but not other immune cells in B16 (Fig. 1, C and D). Notably, *Zbtb32* exhibited a similar expression pattern in B16 and human cancers, overlapping with that of *Havcr2* and *Gzmb* but not *Tcf7* in $CD8^+$ TILs (Fig. 1, E–G). To confirm these results, we sorted two $CD8^+$ TIL subsets, marked by Ly108 and Tim-3, representing T_{pex} and T_{tex}, respectively, from B16-OVA tumor-bearing mice. Quantitative RT-PCR (RT-qPCR) results indicated increased *Zbtb32* mRNA levels in T_{tex} compared with T_{pex} (Fig. 1 H).

Collectively, these findings indicate that *Zbtb32* is selectively expressed by T_{tex} cells, suggesting a potential role in T cell–mediated anti-tumor function.

Zbtb32 expression is regulated by CD28 signaling

To understand the regulation and function of *Zbtb32* expression in murine $CD8^+$ T cells, we constructed *Zbtb32* germline knockout ($Zbtb32^{-/-}$) mice and validated efficient gene knockout efficiency (Fig. S2 A). We initially activated naïve $CD8^+$ T cells with anti-CD3 and CD28 *in vitro* and collected samples at various time points to assess *Zbtb32* mRNA levels. Results showed that *Zbtb32* expression levels were increased at 48 h after T cell activation and peaked around 2–3 days compared with the naïve state, indicating induction of *Zbtb32* expression following T cell activation (Fig. 2 A). To delineate the specific activation signals underlying Zbtb32 regulation, we activated WT naïve $CD8^+$

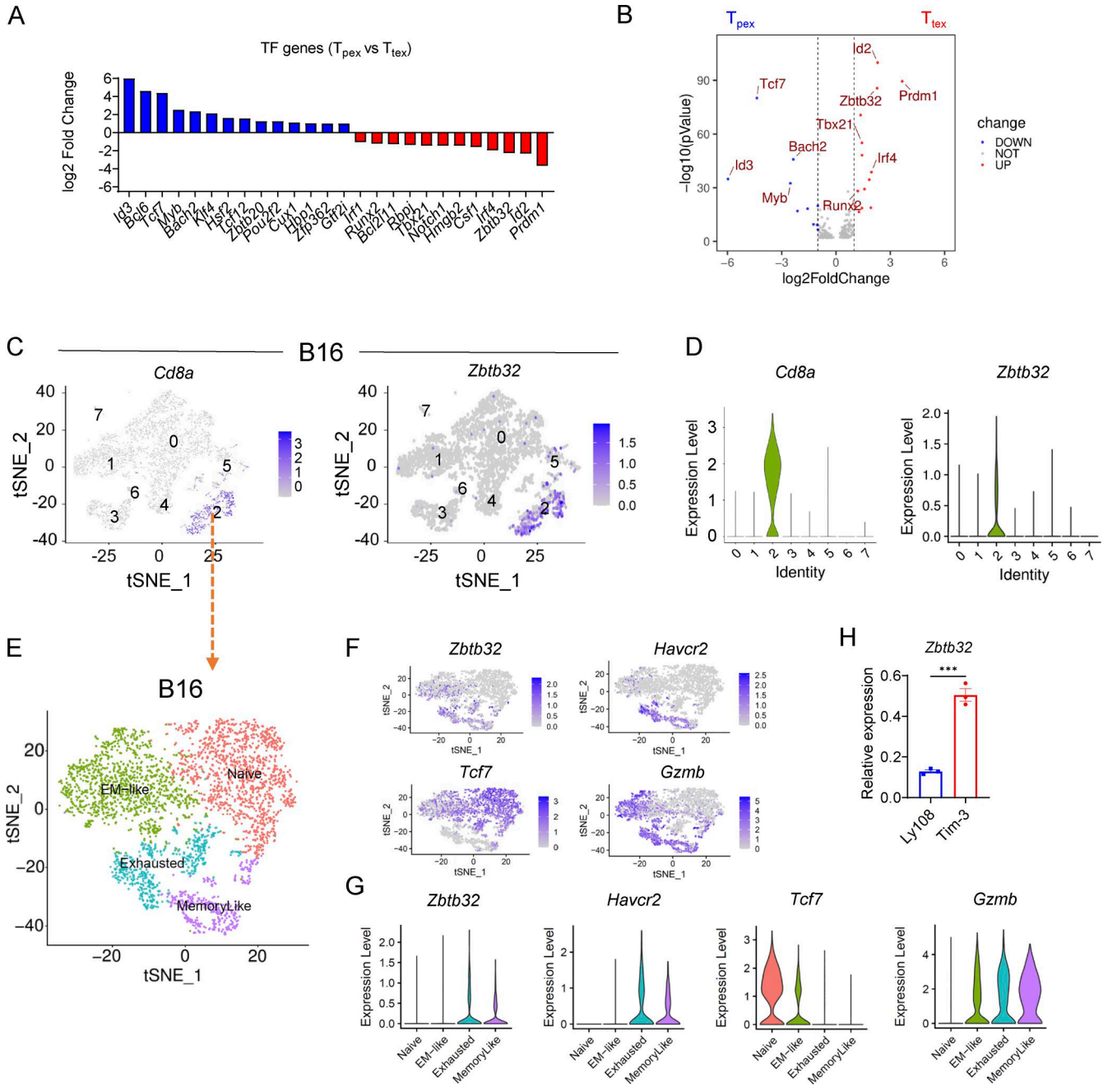

Figure 1. ***Zbtb32* expression is selectively upregulated in T_{tex} tumor-infiltrating CD8⁺ T cells. (A)** Fold change in the expression level of different TFs in T_{pex} and T_{tex} OT-I TILs in E.G7. **(B)** Volcanic plot showing the differential expression of TFs between T_{pex} and T_{tex} OT-I TILs in E.G7. **(C)** FeaturePlots showing *Cd8a* and *Zbtb32* expression profiles in B16 TILs. **(D)** The expression levels of *Zbtb32* and *Cd8a* in different clusters of B16 TILs. **(E)** The tSNE plot of scRNA-seq dataset, indicating global transcriptomic similarities of CD8⁺ TILs in B16 TME. **(F)** FeaturePlots showing expression profiles of *Zbtb32* and other classic genes in B16 CD8⁺ TILs. **(G)** *Zbtb32* and other classic genes expression levels in different clusters of B16 CD8⁺ TILs. **(H)** RT-qPCR analysis of *Zbtb32* expression in Ly108⁺ and Tim-3⁺ CD8⁺ TILs (n = 3 for each group). GEO accessions: (A and B) GSE182035, (C–G) GSE122675. Unpaired two-tailed Student's t test (H), ***P < 0.001. Data shown are a representative of at least two independent experiments.

T cells under varying concentrations of anti-CD3 or anti-CD28 for 3 days to assess *Zbtb32* expression. The results revealed that *Zbtb32* expression levels exhibited dose-dependent changes only in response to anti-CD28 stimulation, but not to anti-CD3 (Fig. 2 B). To validate this observation, we co-cultured *Zbtb32*$^{-/-}$ and WT naïve CD8⁺ T cells under the same settings. Consistently, the relative ratios of WT versus *Zbtb32*$^{-/-}$ cells responded in a dose-dependent manner only to anti-CD28 administration (Fig. 2 C). Together, these findings indicate that co-stimulatory CD28 signal, rather than TCR signal, predominantly regulates *Zbtb32* expression.

More specifically, we activated CD8⁺ T cells with different signaling inhibitors and collected samples on day 3 for analysis. Since CD8⁺ T cells could secrete a large amount of IL-2 after

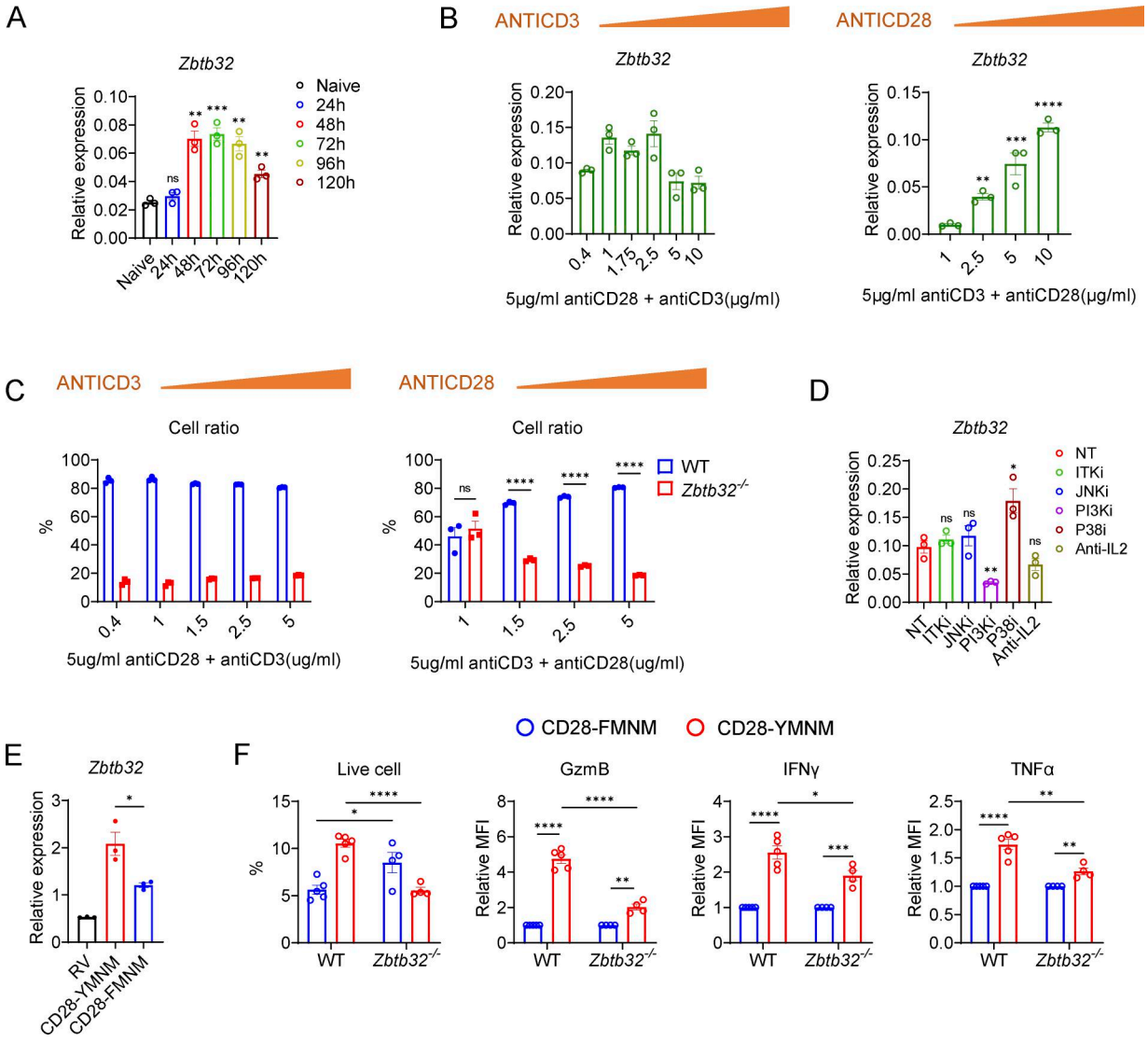

Figure 2. **The CD28-PI3K axis induces *Zbtb32* expression after CD8⁺ T cell activation. (A)** The level of *Zbtb32* expression was measured by RT-qPCR in activated CD8⁺ T cells *in vitro* (n = 3 for each group). **(B)** Quantifications of *Zbtb32* expression levels were measured by RT-qPCR. The cells were activated by gradient dilutions of anti-CD3 plus fixed dilution of anti-CD28 or fixed dilution of anti-CD3 plus gradient dilutions of anti-CD28 (n = 3 for each group). **(C)** Quantifications of co-culture cell ratios of WT versus *Zbtb32*$^{-/-}$ CD8⁺ T cells were measured by flow cytometry. The cells were activated by gradient dilutions of anti-CD3 plus fixed dilution of anti-CD28 or fixed dilution of anti-CD3 plus gradient dilutions of anti-CD28 (n = 3 for each group). **(D)** The *Zbtb32* expression level was measured by RT-qPCR in activated CD8⁺ T cells in the presence of various inhibitors or antibodies (n = 3 for each group). **(E)** The *Zbtb32* expression level was measured by RT-qPCR in CD28-and Y189F mutant CD28 OE CD8⁺ T cells (n = 3 for each group). **(F)** Quantifications of live cell number and relative MFI of GzmB, IFNγ, and TNFa in CD28- and Y189F mutant CD28 OE WT and *Zbtb32*$^{-/-}$ activated CD8⁺ T cells were measured by flow cytometry. The levels in the Y189F mutant CD28 OE group were normalized (n = 5 for each group). Data in all graphs are shown as means ± SEM, *P < 0.05, **P < 0.01, ***P < 0.001, and ****P < 0.0001 by paired or unpaired two-tailed Student's t test. Data shown are a representative of at least two independent experiments.

activation, we also included with anti–IL-2 block antibody. Expectedly, a significant reduction in *Zbtb32* mRNA levels was only noted in cells treated with an inhibitor to PI3K, downstream of CD28 (Fig. 2 D).

We then further assessed CD28-PI3K axis in regulation of *Zbtb32* expression. Since the YMNM motif, especially the 189 tyrosine, in CD28 intracellular domain was essential to bind PI3K, we overexpressed WT CD28-YMNM and mutant CD28-FMNM in CD8⁺ T cells. Remarkably, WT CD28-YMNM induced higher *Zbtb32* expression than mutant CD28-FMNM (Fig. 2 E), suggesting that CD28 signaling effectively augments *Zbtb32* expression in a PI3K-dependent manner. To validate this, we overexpressed WT and mutant CD28 in both WT and *Zbtb32*$^{-/-}$ cells. Overexpression of WT CD28 in CD8⁺ T cells led to increased cell numbers and elevated expression of functional molecules compared with cells expressing mutant CD28 (Fig. 2 F). These effects were more pronounced in WT cells compared with *Zbtb32*$^{-/-}$ cells (Fig. 2 F), indicating that CD28-PI3K axis enhances CD8⁺ T cell effector functions, at least in part, through the upregulation of *Zbtb32* expression.

Zbtb32 is required for optimal CD8⁺ T cell effector function

To assess the roles of Zbtb32 in T cell function, we firstly utilized fluorescence-activated cell sorting (FACS) to examine T cell compartments in primary and secondary lymphoid organs under steady-state condition, in which significant difference was hardly observed in cell populations between *Zbtb32*$^{-/-}$ and WT mice (Fig. S2, B–D), confirming that T cell development and homeostasis remained unaffected after *Zbtb32* deficiency.

Then, to explore the function of Zbtb32 in CD8⁺ T cell activation and function, we isolated naïve CD8⁺ T cells from *Zbtb32*$^{-/-}$ and B6 mice and activated them with anti-CD3/CD28 for 3 days *in vitro*. Analysis revealed reduced T cell activation marker expression in *Zbtb32*$^{-/-}$ T cells, evidenced by decreased CD25⁺CD44⁺ and increased CD62L⁺ populations (Fig. 3, A–C). Additionally, the expression of effector molecules, such as IFNγ and GzmB, was substantially decreased in *Zbtb32*$^{-/-}$ cells, as compared with WT T cells (Fig. 3, A–C). Furthermore, we assessed the apoptosis levels of *Zbtb32*$^{-/-}$ and WT CD8⁺ T cells after 3-day activation, utilizing propidium iodide (PI) and Annexin V as indicators. Notably, *Zbtb32*$^{-/-}$ cells exhibited increased apoptosis compared with WT cells (Fig. 3, D and E). Besides, we evaluated cell proliferative potential by activating CFSE-labeled naïve cells *in vitro* for 3 days. Expectedly, *Zbtb32*$^{-/-}$ cells displayed stronger CFSE signals with fewer rounds of cell division than WT counterparts (Fig. 3 F), indicating compromised proliferation after *Zbtb32* ablation.

Next, to evaluate the cytotoxicity in antigen-specific CD8⁺ T cells in the absence of Zbtb32, we firstly pre-activated *Zbtb32*$^{-/-}$ or WT OT-I cells for 36 h, followed by co-culture with OVA-expressing B16 cells at various effector-to-target (E:T) ratios. To avoid the impact of cell numbers, we also incubated CD8⁺ T cells with IL-2 before co-culture. Using caspase-3 as the indicator of cell death, we observed that almost all cells survived and WT CD8⁺ T cells exhibited stronger killing capacity and higher CD25 expression level compared with *Zbtb32*$^{-/-}$ counterparts (Fig. 3, G and H).

Moreover, to further verify the effector functions of *Zbtb32*$^{-/-}$ or WT T cells *in vivo*, we co-transferred naïve *Zbtb32*$^{-/-}$ and WT OT-I cells into mice infected with OVA-expressing *Listeria monocytogenes* (LM-OVA). *Zbtb32*$^{-/-}$ OT-I cells consistently displayed defects in T cell activation and function, with decreased cell numbers, cytotoxicity, and upregulated CD127 expression, representing increased memory cell proportions, while WT OT-I cells, with robust cytokine secretion and effector function, accompanied with increased KLRG1⁺ population (Fig. 3, I–K).

Collectively, these results demonstrate that Zbtb32 is required for optimal CD8⁺ T cell activation and effector function.

Zbtb32 promotes CD8⁺ T cell–mediated anti-tumor rejection

Upon establishing a pivotal role of Zbtb32 in CD8⁺ T cell function, we next analyzed the differences between *Zbtb32*$^{-/-}$ and WT mice in cancer, using B16-OVA, E.G7, and MC38-GP33 tumor models. Markedly, tumor growth was increased after the ablation of Zbtb32 compared with WT counterparts (Fig. 4 A). Given our focus on melanoma and the single-cell data in B16-OVA tumor models, we chose the B16-OVA model for further investigation.

Then, we quantified the numbers of various immune cell types in B16-OVA TME and observed a decrease only in CD4⁺ and CD8⁺ T cell numbers in *Zbtb32*$^{-/-}$ mice, while other immune cell populations remained relatively unchanged (Fig. S2 E). To ascertain which cell types were important in this anti-tumor process, we selectively depleted CD4⁺ T, CD8⁺ T, or NK cells in mice receiving B16-OVA (Fig. 4 B). Remarkably, the difference between *Zbtb32*$^{-/-}$ and WT mice in tumor volumes was only abolished in the absence of CD8⁺ T cells, but not CD4⁺ T cells or NK cells, when compared with the isotype IgG control group. This result demonstrates that CD8⁺ T cells are the key mediators of tumor rejection regulated by Zbtb32.

Furthermore, we analyzed CD8⁺ TILs in B16-OVA TME. Within the CD8⁺ T cell subset, we observed decreased levels of CD44 and Ki-67 in *Zbtb32*$^{-/-}$ mice (Fig. S2 F), indicating attenuated activation and proliferation. Importantly, IFNγ⁺GzmB⁺ population was significantly reduced in *Zbtb32*$^{-/-}$ mice, likely contributing to their decreased anti-tumor capacity (Fig. S2 G). Additionally, we noted that TCF1⁺ subpopulation was increased by ∼40% in all activated CD8⁺ TILs in *Zbtb32*$^{-/-}$ mice compared with 20% in WT mice (Fig. S2 H).

Subsequently, to further analyze tumor-specific T cells in their differentiation and function, we adoptively transferred naïve *Zbtb32*$^{-/-}$ or WT OT-I or P14 cells into mice subcutaneously inoculated with OVA or GP33-expressing B16-OVA, E.G7, and MC38-GP33 tumor cells (Fig. 4 C). We observed worse survival rates in mice receiving T cells with *Zbtb32* ablation, along with a significant increase in tumor volumes (Fig. 4, D–I). Specifically, *Zbtb32*$^{-/-}$ OT-I cells exhibited impaired T cell function with reduced cell numbers, especially characterized by compromised CD8⁺ T cell differentiation, with TCF1⁺ and Ly108⁺ populations accounting for nearly half of total OT-I TILs (Fig. 4, J and K). In the meantime, these cells exhibited reduced Tim-3⁺ and Cx3CR1⁺ subsets, compared with WT OT-I cells (Fig. 4, J and K). Additionally, *Zbtb32* deficiency led to a significant reduction in IFNγ and GzmB expression, along with a decrease in the level of Ki-67 expression (Fig. 4, J and K), which aligned with the differences observed in *Zbtb32*$^{-/-}$ and WT mice inoculated with tumors.

Similarly, Zbtb32-overexpressing (OE) CD8⁺ cells exhibited augmented function *in vitro*, further supporting our conclusion (Fig. 5 A). RT-qPCR results demonstrated various effectors—but not stem-like gene expression levels were upregulated after overexpression. And more importantly, when transferring WT or Zbtb32 OE OT-I cells into B16-OVA recipients (Fig. 5 B), diminished TCF1⁺ subset, enhanced cytokine expression, and cytotoxicity were observed in Zbtb32 OE cells, likely leading to improved tumor control and survival rates (Fig. 5, C–F).

Collectively, these findings demonstrate that Zbtb32 is vital for effective CD8⁺ T cell–mediated anti-tumor responses.

ICB overcomes *Zbtb32* deficiency in tumor-specific T cells

In light of the previous reports on superior responses by T_{pex} cells to ICB therapy (Wei et al., 2017; Brummelman et al., 2018; Liu et al., 2022), we hypothesized that *Zbtb32*$^{-/-}$ T cells might exhibit improved response to ICB therapy. To investigate this, we treated B16-OVA–bearing mice transferred with *Zbtb32*$^{-/-}$ or WT OT-I naïve cells with or without anti–PD-1 at day 7, 10, and 13

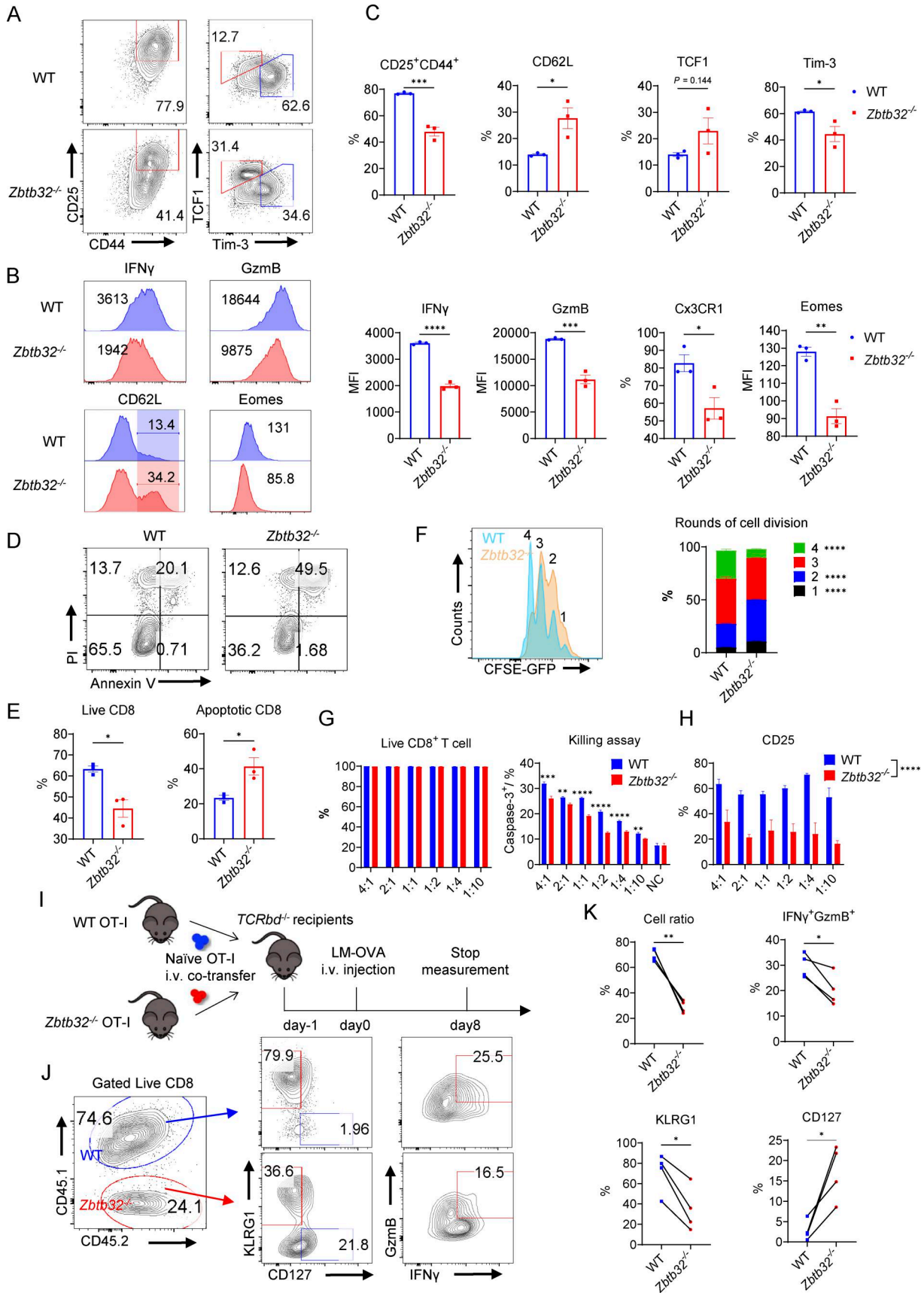

Figure 3. **Zbtb32 augments the short-term immune responses of CD8⁺ T cells. (A)** Representative FACS plots of TCF1 and Tim-3, CD25, and CD44 in WT and *Zbtb32*$^{-/-}$ CD8⁺ cells activated *in vitro*. **(B)** Histogram plots (left panel) and MFI (right panel) of IFNγ and GzmB in WT and *Zbtb32*$^{-/-}$ CD8⁺ cells activated

in vitro. **(C)** Quantifications of specific molecules in WT and *Zbtb32*$^{-/-}$ CD8$^+$ cells cultured *in vitro* (n = 3 in each group). **(D)** Representative plots of PI and Annexin V in WT and *Zbtb32*$^{-/-}$ CD8$^+$ cells cultured *in vitro*. **(E)** Quantifications of PI and Annexin V in WT and *Zbtb32*$^{-/-}$ CD8$^+$ cells cultured *in vitro* (n = 3 in each group). **(F)** Representative plots and quantifications of CFSE expression level in WT or *Zbtb32*$^{-/-}$ CD8$^+$ T cells cultured *in vitro* for 3 days (n = 8 in each group). **(G)** The quantifications of caspase-3 expression in B16-OVA cells and live cell percentages of activated WT or *Zbtb32*$^{-/-}$ CD8$^+$ T cells under different E:T ratios in a co-culture killing assay (n = 5 in each group). **(H)** Expressions of CD25 in activated WT or *Zbtb32*$^{-/-}$ CD8$^+$ T cells under different E:T ratios in a co-culture killing assay with B16-OVA cells (n = 3 in each group). **(I)** Schematic representation of the co-transfer of 1.5 × 10^5 WT and 1.5 × 10^5 *Zbtb32*$^{-/-}$ naïve OT-I cells into *TCRbd*$^{-/-}$ mice infected with 1 × 10^5 CFU of LM-OVA (n = 4 in each group). **(J)** Representative FACS plots of KLRG1 and CD127, IFNγ, and GzmB expressions in WT and *Zbtb32*$^{-/-}$ OT-I cells (n = 4 in each group). **(K)** Quantifications of cell ratio of WT, *Zbtb32*$^{-/-}$ OT-I cells, KLRG1 and CD127, and IFNγ$^+$GzmB$^+$ expressions in WT and *Zbtb32*$^{-/-}$ OT-I cells (n = 4 in each group). Data in all graphs are shown as means ± SEM, *P < 0.05, **P < 0.01, ***P < 0.001, and ****P < 0.0001 by paired or unpaired two-tailed Student's t test. Data shown are a representative of at least two independent experiments.

posttumor inoculation (Fig. 6 A). Tumor volume evaluations revealed *Zbtb32*$^{-/-}$ OT-I cells had worsened tumor control ability compared with WT OT-I cells. However, both of them displayed improved tumor control upon ICB treatment, while mice with *Zbtb32*$^{-/-}$ T cells exhibited stronger enhancement than those with WT cells, resulting in similar tumor volumes between two groups of recipients (Fig. 6, B and C). This illustrates that ICB treatment eliminated the defects in tumor control caused by *Zbtb32* deficiency.

To gain additional insights in this change, we examined the cellular characteristics with or without ICB treatment. Notably, ICB treatment did not significantly alter the proportions of T_{pex} and T_{tex} cells, wherein *Zbtb32*$^{-/-}$ OT-I cells consistently exhibited increased ratios of TCF1$^+$ and Ly108$^+$ populations (Fig. 6, D and E), indicative of enhanced stem-like attribute and maintenance of stemness. Then, statistical analysis revealed that ICB treatment significantly increased T cell numbers, particularly in *Zbtb32*$^{-/-}$ OT-I cells, which expanded dramatically to the comparable levels with WT cells (Fig. 6 F). Moreover, substantial increases in cell numbers of both TCF1$^+$ and Tim-3$^+$ populations were observed in anti–PD-1–treated *Zbtb32*$^{-/-}$ T cells, while those in WT counterparts remained largely unchanged, suggesting a greater impact of the ICB on *Zbtb32*$^{-/-}$ T cell numbers (Fig. 6 F).

Furthermore, the assessment of Ki-67 mean fluorescence intensity (MFI) and cytokine secretion, particularly IFNγ, GzmB, and IL-2, gave similar conclusions. The ICB treatment significantly enhanced proliferation and cytokine release in *Zbtb32*$^{-/-}$ T cells, without much impact on WT counterparts (Fig. 6, G–I), providing compelling evidence for the restoration of the antitumor response in *Zbtb32*$^{-/-}$ cells with ICB treatment. Additionally, there was no evident change in T cells in draining LNs (DLNs) (Fig. 6 J), likely due to low *Zbtb32* expression levels in T_{pex} cells there.

Our results together show that the impairments in antitumor function of T cells resulted from *Zbtb32* deficiency could be largely rescued after anti-PD1 treatment, associated with T_{pex} expansion and differentiation into T_{tex}.

Zbtb32 transcriptionally regulates CD8$^+$ T cell function in tumor

To understand the molecular regulation of CD8$^+$ T cells by Zbtb32 in cancer, we inoculated B16-OVA cells the day after co-transferring *Zbtb32*$^{-/-}$ and WT naïve OT-I cells into *TCRbd*$^{-/-}$ mice and sacrificed the recipients at day 30 (Fig. 7 A). Consistent with separate OT-I–adoptive cell transfer experiment, compromised CD8$^+$ T cell numbers and the changes in TCF1$^+$ and Tim-3$^+$ frequencies were found due to *Zbtb32* deficiency. T cell function and expansion was severely decreased as a result of *Zbtb32* deletion, accompanied by reduced IFNγ and GzmB expression and MFI of Ki-67 (Fig. 7, B and C), indicating an indispensable role of Zbtb32 in tumor-specific CD8$^+$ T cell function. Interestingly, similar difference was not observed in cell numbers or marker expression in DLNs and spleen (SPL) (Fig. S3, A and B), suggesting that the impact of *Zbtb32* deficiency may be limited to the TILs.

To further explore Zbtb32 function over the course of tumor development, we compared CD8$^+$ TILs at early and late phases. The results revealed that the differences between *Zbtb32*$^{-/-}$ and WT T cells in cell numbers and T cell subsets became more dramatic over time (Fig. S3, C–E). Then to analyze Zbtb32 function, we performed RNA-seq on FACS-sorted *Zbtb32*$^{-/-}$ and WT CD8$^+$ TILs at day 30 after co-transfer in CD45.1$^+$ recipients. Differentially expressed genes (DEGs) indicated downregulation of effector- and terminal-associated genes (*Id2*, *Havcr2*, *Batf*, *Prdm1*, *Eomes*, and *Tigit*), co-stimulatory or cytokine receptors (*Il2ra*, *Il2rb*, *CD28*, *CD69*, and *Icos*), and cytokines (*Ifng*, *Il12*, *Il21*, and granzyme family) in *Zbtb32*$^{-/-}$ cells, with upregulation of progenitor-associated genes (*Id3*, *Bcl6*, *Tcf7*, *Sell*, and *Cxcr5*), compared with WT T cells (Fig. 7, D and E). Gene ontology (GO) enrichment analysis unveiled the prominent presence of effector-related and proliferative pathways in WT cells (Fig. 7 F), underscoring a critical role of Zbtb32 in facilitating CD8$^+$ T cell activation and functional differentiation. Furthermore, gene set enrichment analysis (GSEA) unveiled distinct patterns of gene expression between *Zbtb32*$^{-/-}$ and WT OT-I cells, in which genes upregulated in the T_{pex} population were more enriched in *Zbtb32*$^{-/-}$ OT-I cells, while those associated with the T_{tex} phenotype were predominantly concentrated in WT OT-I cells (Fig. 7 G).

Since the results of above experiments may be impacted by the changes of T_{pex} and T_{tex} cell ratios, we directly compared these subsets in the presence or absence of *Zbtb32*. We repeated the co-transfer assay (Fig. S4 A) and specifically analyzed the expression levels of effector molecules (IFNγ, GzmB, and Ki-67) within T_{pex} and T_{tex} subsets. Consistent with our previous results, WT TILs displayed a stronger bias toward terminal differentiation (Fig. S4, B and C). Moreover, both WT T_{pex} and T_{tex} cells exhibited higher expression levels of effector markers compared with Zbtb32-deficient counterparts (Fig. S4, B and C). For further investigation, we sorted WT and *Zbtb32*$^{-/-}$ T_{tex} TILs from B16-OVA tumor-bearing CD45.1 mice and performed RNA-seq analysis. WT T_{tex} cells expressed elevated levels of molecules

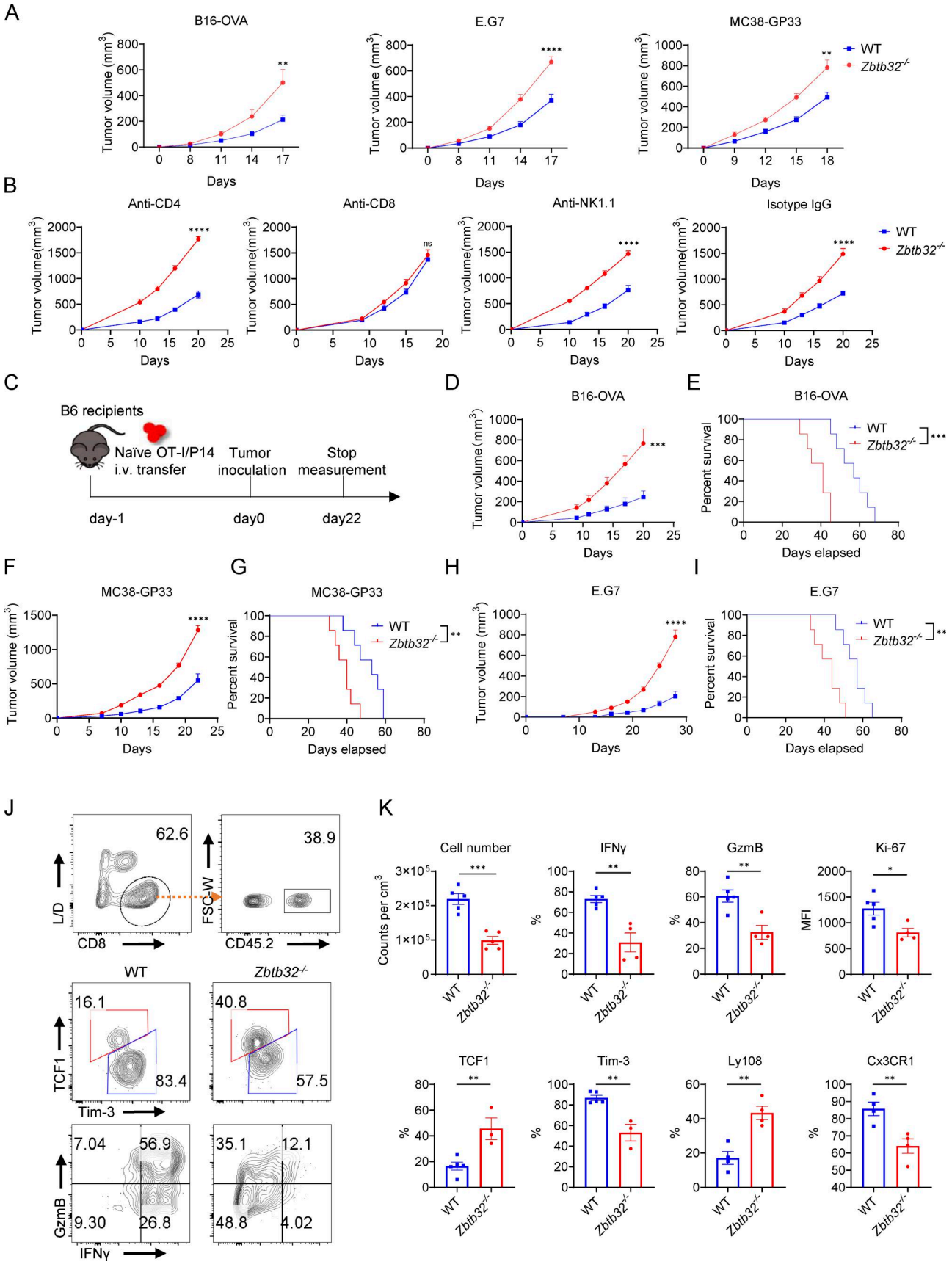

Figure 4. **Loss of Zbtb32 inhibits the anti-tumor response of CD8⁺ T cells. (A)** Tumor growth in WT and *Zbtb32*$^{-/-}$ mice after transplantation of 1 × 10^6 B16, E.G7, or MC38 cells (n = 6 for each group). **(B)** Tumor growth in WT and *Zbtb32*$^{-/-}$ mice depleted of CD4⁺, CD8⁺, or NK cells after transplantation of 0.5 × 10^6 B16

cells (n = 6 for each group). **(C)** Schematic diagram of the transfer of naïve OT-I or P14 cells. **(D)** Tumor growth in mice transplanted with 1 × 10^6 B16-OVA cells after the transfer of 0.3 × 10^6 naïve WT or *Zbtb32*$^{-/-}$ OT-I cells (n = 6 for each group). **(E)** Survival rates of mice transplanted with 1 × 10^6 B16-OVA cells after transfer of 0.3 × 10^6 naïve WT or *Zbtb32*$^{-/-}$ OT-I cells (n = 6 for each group). **(F)** Tumor growth and survival rate in mice transplanted with 1 × 10^6 MC38-GP33 cells after transfer of 0.5 × 10^6 naïve WT or *Zbtb32*$^{-/-}$ P14 cells (n = 5 for each group). **(G)** Survival rate of mice transplanted with 1 × 10^6 B16-OVA cells after transfer of 0.3 × 10^6 naïve WT or *Zbtb32*$^{-/-}$ OT-I cells (n = 5 for each group). **(H)** Tumor growth and survival rate in mice transplanted with 1 × 10^6 E.G7 cells after transfer of 1 × 10^6 naïve WT or *Zbtb32*$^{-/-}$ OT-I cells (n = 5 for each group). **(I)** The survival rate of mice transplanted with 1 × 10^6 MC38-GP33 cells after transfer of 0.5 × 10^6 naïve WT or *Zbtb32*$^{-/-}$ P14 cells (n = 5 for each group). **(J)** Representative FACS plots of the gating strategy (upper panel), TCF1 and Tim-3 (middle panel), and IFNγ and GzmB (lower panel) expressions in WT and *Zbtb32*$^{-/-}$ OT-I TILs in B16-OVA TME. **(K)** Quantifications of cell number and specific molecules of WT and *Zbtb32*$^{-/-}$ OT-I TILs in B16-OVA TME (n = 5 for each group). Data are shown as means ± SEM, *P < 0.05, **P < 0.01, ***P < 0.001, and ****P < 0.0001 by unpaired two-tailed Student's t test (K), Bonferroni-corrected two-way ANOVA (A, B, D, F, and H), and Mantel–Cox test (E, G, and I). Data shown in all graphs are a representative of two to three independent experiments.

representing CD8$^+$ T cell activation, proliferation and terminal differentiation, and enriched for the pathways associated with T cell regulation (Fig. S4, D–F).

Of note, GSEA revealed that within T_{tex} population, WT OT-I TILs still displayed heightened expression of T_{tex} signature genes compared with *Zbtb32*$^{-/-}$ OT-I TILs (Fig. 7 H), indicating that Zbtb32 not only affects CD8$^+$ T cell differentiation but also critically regulates effector gene expression in TME. However, the transcriptional differences between WT and *Zbtb32*$^{-/-}$ T_{pex} cells were less pronounced than those observed in T_{tex} cells (Fig. 7 H). We speculate it is due to the relatively low expression levels of *Zbtb32* in T_{pex} cells.

Additionally, transposase-accessible chromatin with high-throughput sequencing (ATAC-seq) analysis was conducted on co-transferred *Zbtb32*$^{-/-}$ and WT OT-I cells in B16-OVA tumors. The results indicated that like other typical transcriptional regulators, Zbtb32 probably directly regulated gene transcription initiation, with the accessibility of promoter regions comprised by more than half of the differentially accessible regions (Fig. 8, A and B). While *Zbtb32* deficiency did not globally abrogate chromatin accessibility, genes in the pathways regulating T cell function exhibited specifically increased accessibility in WT cells (Fig. 8, C and D). In several genes, whose promoter regions exhibited differential chromatin accessibility, genes associated with effector-like and terminal differentiation (*Gzmk*, *Il2ra*, *Il2rb*, *Havcr2*, *Pdcd1*, and *Cd69*) were less accessible in *Zbtb32*$^{-/-}$ OT-I cells, while those highly expressed in T_{pex} population with suppression activities on T_{tex} differentiation (*Bcl6*, *Id3*, and *Myb*) showed the opposite trends (Fig. 8 E). Peak set enrichment analysis revealed enrichment of T_{pex} and stem-like CD8$^+$ T cell epigenetic signatures in *Zbtb32*$^{-/-}$ cells, contrasting with T_{tex} cell signatures in WT cells (Fig. 8 F).

In summary, our results highlight a pivotal role of Zbtb32 in the regulation of CD8$^+$ T cells in their differentiation and effector function.

Antagonizing function of Zbtb32 and Bcl6 in CD8$^+$ T cells

To understand the potential role of Zbtb32, we conducted chromatin immunoprecipitation sequencing (ChIP-seq) of Zbtb32 using CD8$^+$ T cells activated *in vitro* for 4 days. The analysis of ChIP-seq results revealed that Zbtb32 might exert its function through binding to various DNA regions, with a considerable portion at the promoter regions (Fig. S5 A). Known motif analysis indicated a strong similarity between the binding motifs of Zbtb32 and several factors involved in regulating CD8$^+$ T cell function, such as BATF, JunB, IRF4, Fli1, T-bet, and RUNX2 (Fig. S5 B), suggesting Zbtb32 may also participate in this process.

Bcl6 has been shown to be highly expressed by T_{pex} and functions to promote T_{pex} program in TME (Sun et al., 2023a; Wu et al., 2016). It thus appears that belonging to the same family, the functional roles of Zbtb32 and Bcl6 are not similar, but rather opposite. Based on our previous work (Sun et al., 2023a), GSEA analysis indicated that genes enriched in the Bcl6$^+$ T_{pex} population were mostly associated with *Zbtb32*$^{-/-}$, but not WT T cells (Fig. S5 C), indicating that these two factors might have distinct function in regulating CD8$^+$ T cell subsets in TME. To explore the functional relationship of Bcl6 with Zbtb32, we integrated the ChIP-seq results of Zbtb32 with those of Bcl6 and other pivotal TFs regulating T cell exhaustion or enriched in motif analysis (Blimp1, TCF1, T-bet, and BATF). Particularly, predictions of TF-binding motifs revealed nearly identical top motifs for Zbtb32 and Bcl6 (Fig. 9 A). Remarkably, among these factors, Bcl6 exhibited highest overlap with Zbtb32 in their genome-wide occupancy (Fig. 9 B). Additionally, peak overlap diagrams and density maps illustrated striking similarities in their bindings on exhaustion-related gene loci (Fig. 9 C). However, this resemblance was not observed in other core factors, like Blimp1 and TCF1, which have been implicated in determining the fate of CD8$^+$ TILs in TME (Fig. 9 C). These data strongly suggest functional interactions between Bcl6 and Zbtb32.

To further investigate the interplay between Zbtb32 and Bcl6, we integrated their ChIP-seq data with RNA-seq results to identify potential target genes regulated by both factors (Fig. S5 D). First, we identified genes directly induced or suppressed by Zbtb32 or Bcl6. Next, we integrated these findings with DEGs in TCF1$^+$ T_{pex} and TCF1$^-$ T_{tex} TILs to compare their roles in T cell exhaustion. Notably, genes induced by Zbtb32 and suppressed by Bcl6 were predominantly enriched in the T_{tex} subset, while Zbtb32-suppressed and Bcl6-induced genes were mostly enriched in the T_{pex} subset. Among these exhaustion-associated genes, we identified numerous critical molecules regulated by both of them. Furthermore, more than half of the genes induced or suppressed by Zbtb32 were inversely regulated by Bcl6, highlighting their opposing roles in the CD8$^+$ T cell regulatory network.

To confirm this, we separately or simultaneously overexpressed Zbtb32 and Bcl6 in OT-I cells and co-transferred them

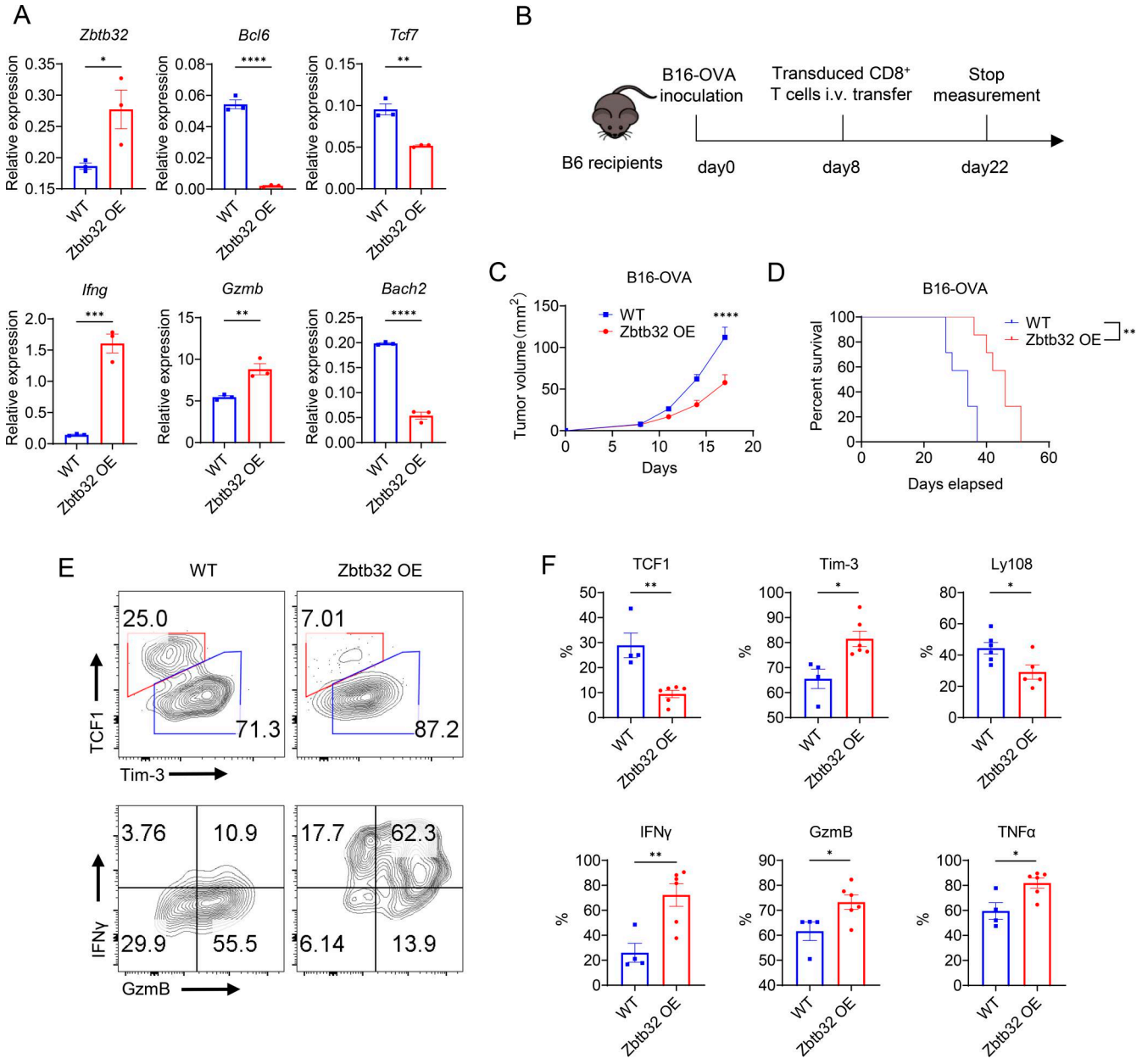

Figure 5. **Zbtb32 overexpression enhances CD8⁺ T cell anti-tumor rejection. (A)** Quantifications of specific genes expressions in WT, Zbtb32 OE activated CD8⁺ T cells measured by RT-qPCR (n = 3 for each group). **(B)** Schematic diagram of the transfer with 7 × 10^5 transduced OT-I or P14 cells on day 8. **(C)** Tumor growth in mice transferred with 7 × 10^5 activated Zbtb32 OE or RV control CD8⁺ OT-I cells on 8 days after 1 × 10^6 B16-OVA cells inoculation (n = 6 for each group). **(D)** Survival rate in mice transferred with 7 × 10^5 activated Zbtb32 OE or RV control CD8⁺ OT-I cells on day 8 after 1 × 10^6 B16-OVA cells inoculation (n = 6 for each group). **(E)** Representative plots of TCF1 and Tim-3, IFNγ and GzmB in RV control, and Zbtb32 OE CD8⁺ OT-I TILs in B16-OVA TME. **(F)** Quantifications of specific molecules in RV control and Zbtb32 OE CD8⁺ OT-I TILs in B16-OVA TME (n = 6 for each group). Data are shown as means ± SEM; ns, not significant; *P < 0.05, **P < 0.01, ***P < 0.001, and ****P < 0.0001 by unpaired (A and F) two-tailed Student's t test, Bonferroni-corrected two-way ANOVA (C), and Mantel–Cox test (D). Data shown in all graphs are a representative of three independent experiments.

with control OT-I cells into B16-OVA recipients. Single overexpression of Zbtb32 enhanced, but that of Bcl6 impaired, CD8⁺ T cell function (Fig. S5 E). However, in doubly overexpressed T cells, there was no significant difference in cell numbers, cytotoxic molecule expression, and cell differentiation compared with control infected T cells (Fig. S5 E). Moreover, this conclusion was supported by B16-OVA recipients adoptively transferred with *Zbtb32*$^{-/-}$, *Bcl6*$^{-/-}$ single-knockout, and *Zbtb32*$^{-/-}$*Bcl6*$^{-/-}$ double-knockout naive OT-I cells (Fig. S5 F). The tumor volumes observed in mice transferred with double-knockout OT-I cells exhibited moderate differences in tumor control compared with mice receiving *Zbtb32*$^{-/-}$ and *Bcl6*$^{-/-}$ OT-I cells, but with no significant difference from those carrying WT OT-I cells (Fig. S5 G). All these results support the notion that Zbtb32 and Bcl6 antagonize each other in regulating CD8⁺ T cell–mediated anti-tumor capability.

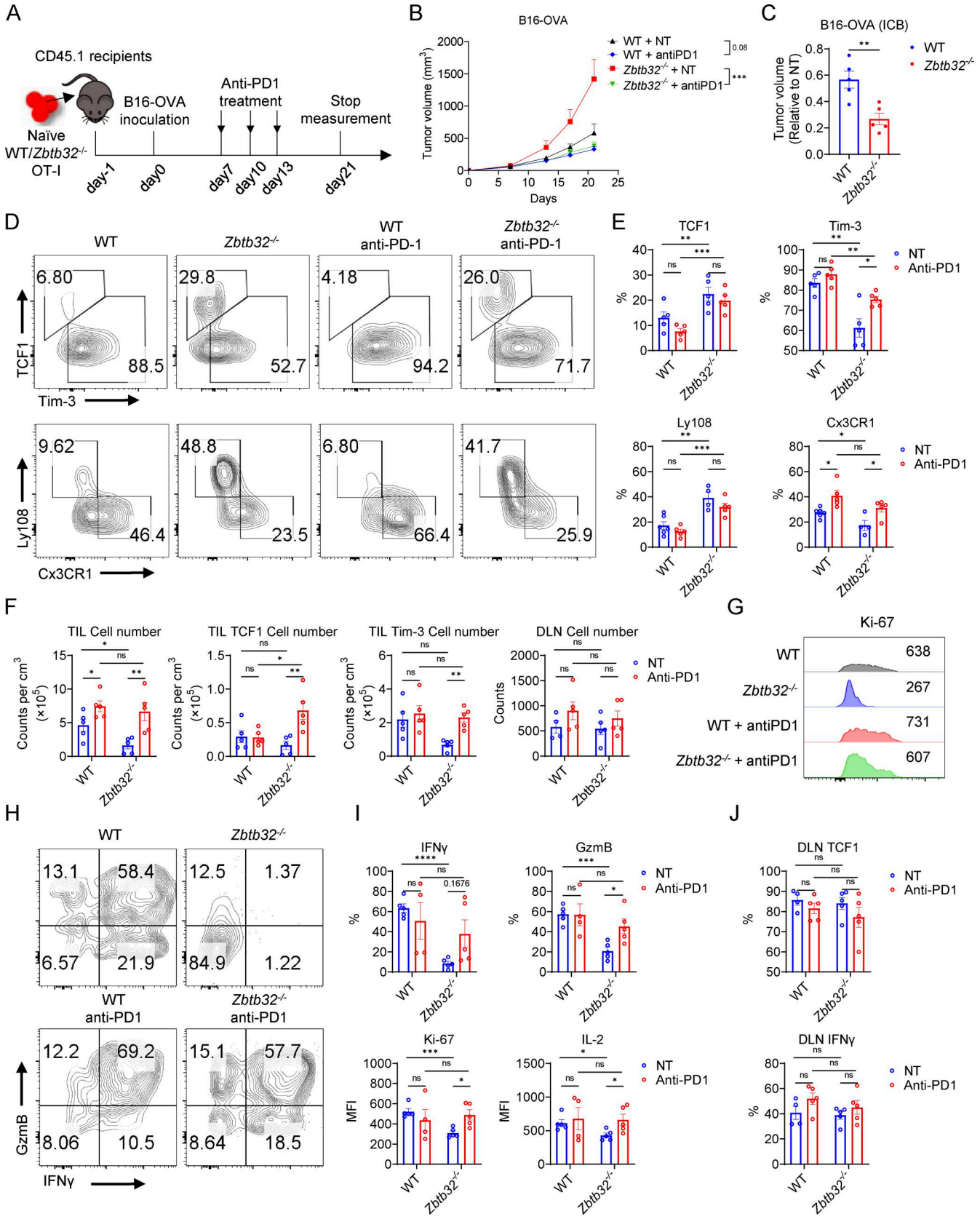

Figure 6. **The impaired tumor control as a result of *Zbtb32* deficiency in T cells is rescued in ICB treatment. (A)** Schematic diagram of anti–PD-1 treatment assay in B16-OVA tumor-bearing mice, transferred with 3 × 10^5 WT or 3 × 10^5 *Zbtb32*$^{-/-}$ naïve OT-I cells before 1 × 10^6 B16-OVA cells inoculation. **(B)** Tumor growth in mice transplanted with 1 × 10^6 B16-OVA cells after the transfer of 0.3 × 10^6 naïve WT or *Zbtb32*$^{-/-}$ OT-I cells, with or without anti–PD-1 treatment (n = 6 for each group). **(C)** Comparison of tumor volumes in WT and *Zbtb32*$^{-/-}$ mice treated with ICB with those in untreated mice. **(D)** Representative

plots of TCF1 and Tim-3, Ly108, and Cx3CR1 expression in WT and *Zbtb32*$^{-/-}$ OT-I TILs with or without anti-PD1 treatment. **(E)** Expressions of TCF1 and Tim-3, Ly108, and Cx3CR1 in WT and *Zbtb32*$^{-/-}$ OT-I TILs with or without anti–PD-1 treatment (n = 6 for each group). **(F)** Quantifications of cell number, T_{pex} and T_{tex} cell number in WT and *Zbtb32*$^{-/-}$ OT-I in TME or DLN with or without anti-PD1 treatment (n = 6 for each group). **(G)** MFI for Ki-67 in WT and *Zbtb32*$^{-/-}$ OT-I in TME with or without anti-PD1 treatment. **(H)** Representative plots of IFNγ and GzmB expression in WT and *Zbtb32*$^{-/-}$ OT-I TILs with or without anti-PD1 treatment. **(I)** Expressions of IFNγ, GzmB, MFI of Ki-67 and IL-2 in WT and *Zbtb32*$^{-/-}$ OT-I in TME with or without anti-PD1 treatment (n = 6 for each group). **(J)** Expression of TCF1 and IFNγ in WT and *Zbtb32*$^{-/-}$ OT-I in DLN with or without anti–PD-1 treatment (n = 6 for each group). Data are shown as means ± SEM; ns, not significant; *P < 0.05, **P < 0.01, ***P < 0.001 and ****P < 0.0001 by Bonferroni-corrected two-way ANOVA (B), unpaired two-tailed Student's t test (C, E, F, I, and J). Data shown in all graphs are a representative of two independent experiments.

Moreover, considering their significant co-occupancy in the genome yet opposing regulations, we attempted to determine whether Zbtb32 and Bcl6 might compete for DNA binding. We firstly compared their binding peaks from their ChIP-seq data and observed substantial overlap at shared sites, particularly in genes essential for CD8$^+$ T cell exhaustion (Fig. S5 H). Analysis of the genome-wide landscape of DNA binding by Zbtb32 before and after Bcl6 overexpression, along with WT and *Zbtb32*$^{-/-}$ ATAC-seq data, revealed that the binding of Zbtb32 at loci of T_{tex}-related genes (*Prdm1*, *Gzmb*, *Havcr2*, and *Gzmk*) diminished or vanished following Bcl6 overexpression (Fig. 9 D).

To verify this discovery, we performed a Zbtb32 ChIP-qPCR assay in CD8$^+$ T cells following 4-day activation, pulling down Zbtb32 before and after Bcl6 overexpression, assessing the binding of Zbtb32 at loci of genes upregulated by Zbtb32 but downregulated by Bcl6 (*Gzmb*, *Havcr2*, *Prdm1*) (Sun et al., 2023a). The results demonstrated that Bcl6 severely dampened Zbtb32 recruitment to these loci through competitive DNA binding (Fig. 9 E). Additionally, we examined the expression levels of these genes to determine if their expressions were influenced by this competition. qPCR results further validated that Bcl6 overexpression reduced the transcriptional levels of these genes (Fig. S5 I), consistent with their downregulations in Bcl6$^+$ CD8$^+$ TILs in our previous finding (Sun et al., 2023a).

Differing from Blimp1, which antagonizes Bcl6 through binding at different sites, Zbtb32 has a highly similar binding preference to Bcl6. To elucidate the differential gene regulation of Zbtb32 and Bcl6, we swapped the BTB domains of Zbtb32 and Bcl6, which recruit cofactors to regulate gene expression. Thus, we overexpressed Zbtb32, Bcl6, and Zbtb32 with the Bcl6 BTB domain (Zbtb-B) and Bcl6 with the Zbtb32 BTB domain (Bcl6-Z) in OT-I cells and transferred them into B16-OVA recipients (Fig. 9 F). Consistently, Zbtb32 OE cells exhibited enhanced tumor control ability, but strikingly, after swapping, the role of Zbtb32 in supporting CD8$^+$ T cell anti-tumor rejection was attenuated in Zbtb32-B OE cells (Fig. 9 G). However, on the other hand, Bcl6 OE cells, which were defective in CD8$^+$ T cell function, were partially rescued in Bcl6-Z OE cells, resulting in a similar anti-tumor capability with Zbtb32-B OE cells (Fig. 9 G). Moreover, we examined their regulation on *Prdm1* expression, negatively regulated by Bcl6 (Johnston et al., 2009; Crotty et al., 2010; Vasanwala et al., 2002), and found that while Bcl6 OE obviously inhibited *Prdm1* expression compared with Zbtb32 OE, Bcl6-Z OE sharply augmented its expression level by tens of times, but in Zbtb32-B OE cells, the level of *Prdm1* decreased substantially (Fig. S6 J).

Furthermore, we co-transferred these four populations with WT OT-I cells into B16-OVA tumor-bearing mice (Fig. 9 H). Evidently, there were relatively higher numbers of Bcl6-Z OE cells than Bcl6 OE cells, while Zbtb32-B OE cells were sharply reduced to a level similar to Bcl6 OE cells (Fig. 9 I). Additionally, while Bcl6 OE inhibited GzmB secretion, Bcl6-Z OE enhanced its level compared with control cells (Fig. 9 J).

The above experiments indicate that Bcl6 and Zbtb32, with similar target genes, differ in the function of their BTB domains in CD8$^+$ T cells. NCoR1 is a well-known cofactor directly recruited by the BTB domain of Bcl6. We thus overexpressed Bcl6 or Bcl6-Z in CD8$^+$ T cells. ChIP-qPCR results reflected NCoR1 recruitment at *Prdm1* gene locus following OE Bcl6, but not Bcl6-Z (Fig. 9 K).

Altogether, these data indicate that Zbtb32 and Bcl6 display antagonistic regulations on target genes through competitive DNA binding in CD8$^+$ T cells, mainly due to their different BTB domains, possibly in recruiting different types or amounts of cofactors.

Zbtb32 mediates CD8$^+$ T cell function through regulating *Id2* expression

To further understand how Bcl6 and Zbtb32 antagonism influences CD8$^+$ T cell function and the underlying mechanisms, we compared the expression levels of exhaustion-associated TFs among the DEGs regulated by Zbtb32 and Bcl6, with a particular focus on those downregulated in *Zbtb32*$^{-/-}$ TILs. Our analysis identified *Id2* as a CD8$^+$ T cell exhaustion-related TF with the most significant upregulation mediated by Zbtb32 in T_{tex} cells (Fig. 10 A). Notably, *Id2* was also among the most downregulated TFs in Bcl6$^+$ CD8$^+$ TILs (Fig. 1 A and Fig. S5 D). Previous studies have reported that Bcl6 severely impairs *Id2* expression in T cells (Sun et al., 2023a; Crotty, 2014). Based on these facts, we inferred that *Id2* is a key target through which Bcl6 antagonizes Zbtb32 via competitive DNA binding. To validate this, we analyzed the occupancies of Zbtb32 and Bcl6 at the *Id2* locus, which revealed strong binding peaks for both at the same promoter sites (Fig. 10 B). Furthermore, ChIP-qPCR results in CD8$^+$ T cells after 4-day *in vitro* activation demonstrated the binding of Zbtb32 at these sites was significantly reduced following Bcl6 overexpression (Fig. 10 C). At the mRNA level, *Id2* showed a pattern consistent with other key factors (Fig. 10 D), being markedly upregulated by Zbtb32 but downregulated by Bcl6. On the other hand, we overexpressed Zbtb32 and found *Id2* RNA levels were significantly increased after Zbtb32 overexpression (Fig. 10 E). These findings confirm that Id2 is a major TF subject to competitive binding at its promoter by Zbtb32 and Bcl6, with opposing regulatory effects.

To analyze the role of Id2 in T cell exhaustion, we overexpressed Id2 in WT and *Zbtb32*$^{-/-}$ OT-I cells and transferred them

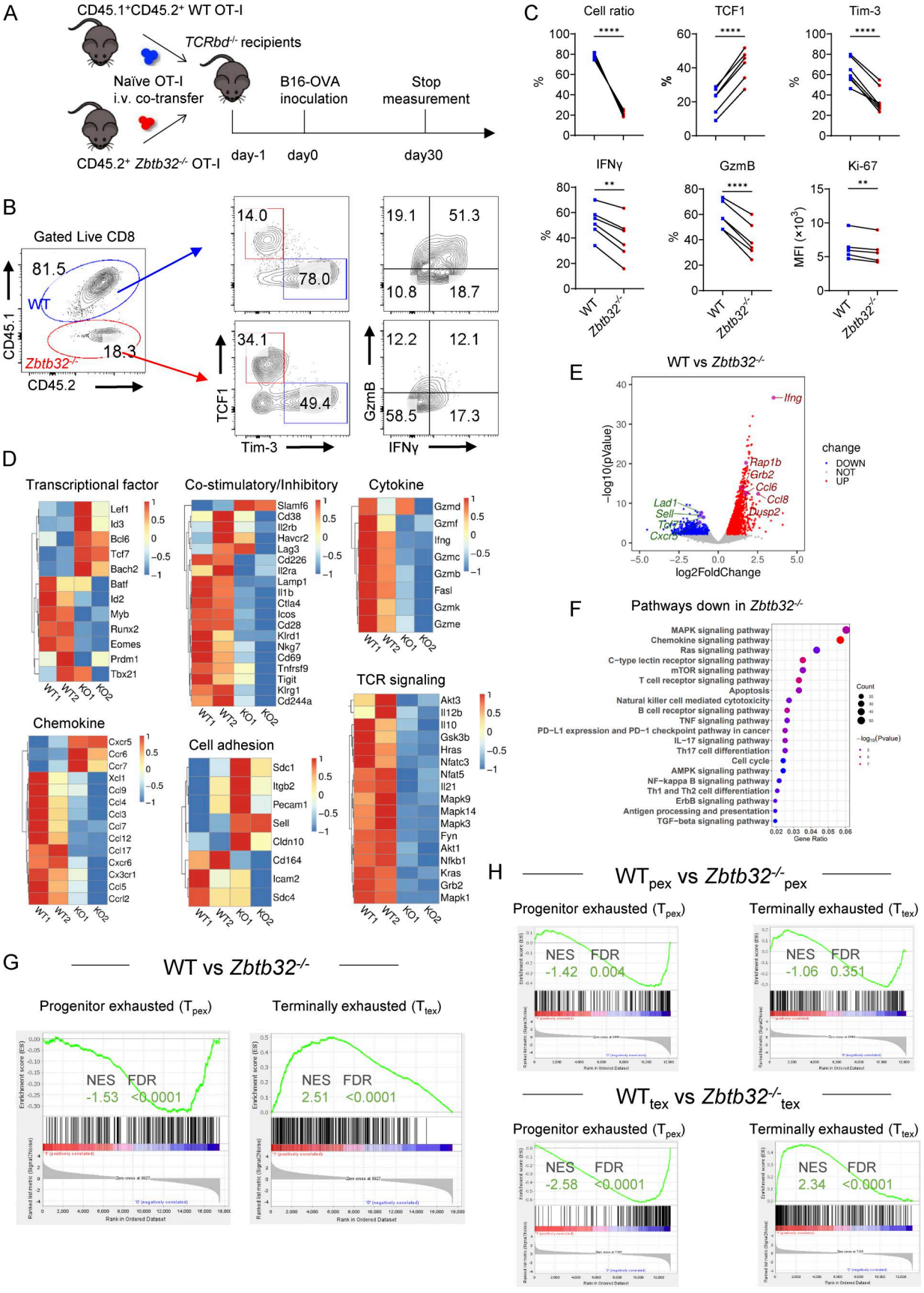

Figure 7. **Zbtb32 transcriptionally regulates tumor-infiltrating CD8⁺ T cell function. (A)** Schematic diagram of the co-transfer of 1.5 × 10^5 WT and 1.5 × 10^5 *Zbtb32*$^{-/-}$ naïve OT-I cells prior to 1 × 10^6 B16-OVA inoculation (n = 6 for each group). **(B)** Representative FACS plots of TCF1 and Tim-3, IFNγ, and GzmB

expression in WT and *Zbtb32*$^{-/-}$ OT-I TILs. **(C)** Quantifications of the cell ratio and specific molecules of WT and *Zbtb32*$^{-/-}$ OT-I TILs. **(D)** Heatmaps showing relative expressions of different signature genes in WT and *Zbtb32*$^{-/-}$ OT-I TILs. **(E)** Volcanic plot showing expression levels of DEGs between WT and *Zbtb32*$^{-/-}$ OT-I TILs. **(F)** Lists of top 20 KEGG biological pathways for DEGs that were downregulated in *Zbtb32*$^{-/-}$ OT-I TILs. **(G)** GSEA analysis for comparing the enrichment DEGs in WT and *Zbtb32*$^{-/-}$ OT-I TILs (GEO accession: GSE114631). **(H)** GSEA analysis for a comparison of the enrichment DEGs in T_{pex} and T_{tex} CD8$^+$ T cell subsets in WT and *Zbtb32*$^{-/-}$ OT-I TILs (GEO accession: GSE114631). Data are shown as means ± SEM; ns, not significant; **P < 0.01 and ****P < 0.0001 by paired two-tailed Student's *t* test (C). Data shown are a representative of at least three independent experiments. NES, normalized enrichment score.

into B16-OVA recipients (Fig. 10 F). Id2 overexpression enhanced anti-tumor control by CD8$^+$ T cell, and importantly, it fully rescued the functional inefficiency of *Zbtb32*$^{-/-}$ CD8$^+$ TILs, reaching the same level as WT cells (Fig. 10 G). Importantly, co-transfer assay further consolidates this observation (Fig. 10 H). Id2 overexpression significantly rescued the impaired tumor control observed following Zbtb32 ablation, as evidenced by the restoration of the T_{pex}/T_{tex} ratio to levels comparable with those in WT cells (Fig. 10 I). Functionally, Id2 partially restored cytotoxicity and proliferative capacity, while IFNγ production remained largely unchanged, both GzmB and Ki-67 expression were notably recovered (Fig. 10 J). These results align well with the known role of Id2 in promoting terminal differentiation and cytotoxic function of TILs (Li et al., 2024).

These findings highlight Id2 as a crucial downstream target upregulated by Zbtb32 to enhance CD8$^+$ T cell–mediated tumor rejection. Moreover, they validate that Zbtb32 is antagonized by Bcl6 in regulating Id2 through competitive DNA binding, leading to different CD8$^+$ T cell fates within TME.

Discussion

CD8$^+$ T cells are crucial for tumor control in cancers. Within the TME, exhausted CD8$^+$ T cells are divided into distinct T_{pex} and T_{tex} subsets, which mediate persistence and effector function in anti-tumor immunity, respectively. A growing body of literature has highlighted the complex regulatory network governing the differentiation and functional fate of tumor-specific CD8$^+$ T cells within the TME (Miller et al., 2019; Li et al., 2024; Sun et al., 2023a; Jung et al., 2022; Chen et al., 2019a; Sun et al., 2023b; Seo et al., 2021; Yao et al., 2021; Jin et al., 2022). However, the mechanisms that fine-tune the balance between T_{pex} and T_{tex} CD8$^+$ TILs remain poorly understood. In this study, we identify Zbtb32 as a key TF necessary for the anti-tumor activity of CD8$^+$ T cells. *Zbtb32* deletion severely impaired the differentiation, proliferation, survival, and cytotoxicity of tumor-specific T cells. Importantly, Zbtb32 directly upregulates Id2 to enhance CD8$^+$ T cell function, which is antagonized by Bcl6.

Persistent antigen stimulation drives CD8$^+$ T cell exhaustion in tumor and chronic infection (Hudson et al., 2019; Utzschneider et al., 2016; Wherry et al., 2007; Jadhav et al., 2019; Im et al., 2016; Das et al., 2017; Niu and Wang, 2023; Chen et al., 2019a; Yao et al., 2021). In LCMV clone 13 infection, virus-specific T cells experience persistent high-level stimulation, resulting in exhaustion characterized by elevated inhibitory signals (Zajac et al., 1998; Wherry et al., 2007). However, TILs targeting tumor self-antigens typically exhibit low TCR affinity due to a diverse repertoire of tumor-reactive CD8$^+$ T cells, the immunosuppressive TME, tumor evasion mechanisms, and interactions with suppressive cells (McMahan et al., 2006; Mognol et al., 2017; Hoffmann and Slansky, 2020). Recent studies suggest that the exhaustion-related transcriptional program is more pronounced in the TME than in chronic infection, indicating distinct transcriptional programs under these two contexts (Tillé et al., 2023). Similarly, we found that *Zbtb32* is primarily expressed in T_{tex} cells, where it promotes CD8$^+$ T cell–mediated tumor rejection. This contrasts with findings in LCMV models, where *Zbtb32* is expressed in T_{pex} cells and suppresses antiviral responses (Miller et al., 2019; Shin et al., 2017). Moreover, Zbtb32 appears to function differently across various cell types, with distinct roles in NK and T cell responses to infections (Beaulieu et al., 2014; Shin et al., 2017). Additionally, IL-12 has been shown to drive *Zbtb32* expression (Adams et al., 2018; Shin et al., 2017), and our findings suggest that CD28 signaling during initial T cell activation may be important to regulate its expression. These results highlight the context-dependent roles of Zbtb32, influenced by specific microenvironmental factors and signaling pathways in different disease models. Further investigations are needed to fully elucidate the underlying mechanisms and their implications.

Although Zbtb32 and Bcl6 belong to the same TF family, our data revealed that they play distinct roles in T cells. Bcl6, a linage regulator in T follicular helper cells (Nurieva et al., 2009; Liu et al., 2013; Choi and Crotty, 2021), represses multiple genes involved in CD4$^+$ T cell development and inhibits CD8$^+$ T cell differentiation and proliferation (Sun et al., 2023a; Liu et al., 2013; Crotty, 2014). We demonstrate that despite shared DNA-binding capabilities, Zbtb32 and Bcl6 regulate CD8$^+$ TILs differently through their BTB domains. While many Zbtb family members are thought to function as repressors (Hoatlin et al., 1999; Miaw et al., 2000), our study reveals that Zbtb32 may also act as an activator. In addition, our findings indicate that *Bcl6* expression is mainly enriched in T_{pex}, whereas *Zbtb32* expression is more prominent in T_{tex} subset. But we also observed the upregulation of Bcl6 in *Zbtb32*$^{-/-}$ T_{tex} TILs, along with reduced effector program. Furthermore, given that Id2 is a well-established mediator of effector function in T_{tex} cells (Li et al., 2024), our identification of Id2 as a downstream target co-regulated by Zbtb32 and Bcl6 and its selective expression in the T_{tex} subset further raised the possibility that in T_{tex} cells, in the absence of Bcl6 expression, Zbtb32 may function primarily through regulating Id2 expression. With the comparison of *Zbtb32*$^{-/-}$*Bcl6*$^{-/-}$ and *Bcl6*$^{-/-}$ mice, the latter still exhibit more effective tumor control (Fig. S5 G), indicating that Zbtb32 can contribute to CD8$^+$ T cell function through Bcl6-independent mechanisms.

Importantly, we identified Id2 as a critical target antagonistically regulated by Zbtb32 and Bcl6, offering novel insights into

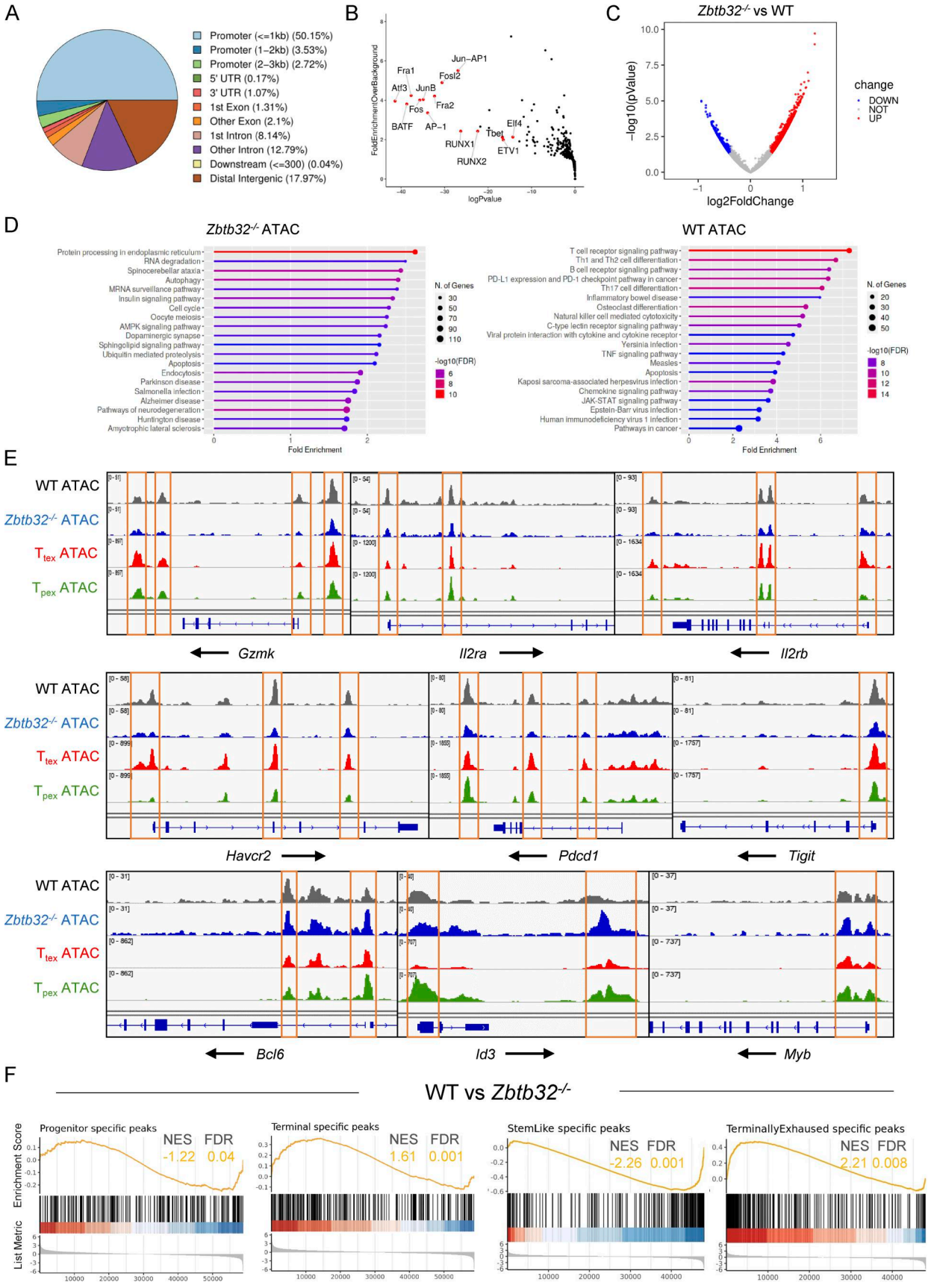

Figure 8. **Zbtb32 regulates the epigenetic landscape of CD8⁺ TILs. (A)** Distribution of differential chromatin accessible regions in WT and *Zbtb32*$^{-/-}$ OT-I TILs across the genome. **(B)** Enrichment of known TF-binding motifs in chromatin accessible regions between WT and *Zbtb32*$^{-/-}$ OT-I TILs. **(C)** Volcanic plot

showing differential chromatin accessible regions between WT and *Zbtb32*$^{-/-}$ OT-I TILs. **(D)** Lists of top 20 GO enrichment pathways for differential chromatin accessible genes in WT and *Zbtb32*$^{-/-}$ OT-I TILs. **(E)** Chromatin accessible peaks at several classic gene loci in WT and *Zbtb32*$^{-/-}$ OT-I TILs aligned with assay for ATAC-seq tracks of T_{tex} and T_{pex} TILs from B16-OVA tumor. Binding peaks on *Prdm1, Batf, Id2, Havcr2, Il2rb, Gzmb*, and *Gzmk* loci are shown (GEO accession: GSE123236). **(F)** PSEA results for a comparison of the enrichment of epigenetic signature peaks in T_{pex} and T_{tex} CD8$^+$ T cell subsets in WT and *Zbtb32*$^{-/-}$ OT-I TILs (GEO accession: GSE123236). PSEA, peak set enrichment analysis.

how these factors govern CD8$^+$ TILs differentiation. Additionally, Id2 is a negative regulator of basic helix–loop–helix (bHLH) transcriptional factors. A previous study reported that Id2 prevents E proteins from enforcing a naïve T lymphocyte gene program (Zook et al., 2018), wherein Id2-deficient cells showed increased enrichment of a canonical bHLH-binding site (E-box motif), suggesting a loss of repression of E protein activity. Notably, HOMER analysis of *Zbtb32*$^{-/-}$ cells also revealed significant enrichment of multiple bHLH motifs (data not shown). These findings support a model in which Zbtb32 promotes Id2 expression to suppress bHLH TF activity, particularly via E-box motif inhibition, thereby regulating the terminal differentiation and effector function of CD8$^+$ TILs.

ICB augments T_{pex} cell numbers and facilitates their conversion to T_{tex} cells (Miller et al., 2019; Im et al., 2016). However, identifying the patients most suitable for ICB stratification remains unclear. In this study, we found that melanoma patients with an abundance of CD8$^+$ T cells but low *ZBTB32* expression had a worse prognosis compared with those with high *ZBTB32* expression. Consistently, mice lacking Zbtb32 exhibited impaired CD8$^+$ T cell function and worsened tumor progression, which could be rescued by ICB treatment, highlighting Zbtb32 as a valuable biomarker for immunotherapy. However, unlike Blimp1 (Sun et al., 2023a), *Zbtb32*$^{-/-}$ cells did not exhibit a better response than WT counterparts following ICB treatment. Our RNA-seq analysis of *Zbtb32*$^{-/-}$ and WT OT-I TILs revealed enhanced expression of T cell effector genes in WT OT-I cells within T_{tex} subset, suggesting that Zbtb32 not only facilitates T_{pex}-to-T_{tex} conversion but also sustains CD8$^+$ T cell function within the TME. Additionally, scRNA-seq analysis showed that *Zbtb32* expression is predominantly enriched in TILs, rather than in DLNs (Carmona et al., 2020; Huang et al., 2022). Our observation that Zbtb32 affects cell numbers in the TME but not in the SPL or DLNs provides additional evidence supporting its role in maintaining CD8$^+$ TIL function, whereas Blimp1 primarily regulates the commitment of T_{tex} from T_{pex} cells. It is noteworthy that, while melanoma patients with low *ZBTB32* expression typically have a worse prognosis, our mouse data indicate that *Zbtb32*-deficient mice are more sensitive to ICB. This suggests a possibility that patients with low *ZBTB32* expression may respond better to ICB, potentially achieving outcomes similar to those with high *ZBTB32* expression. Further investigation is needed in whether low *ZBTB32* expression might serve as a predictor of ICB responsiveness.

Overall, this study focusing on the function of Zbtb32 in CD8$^+$ TILs has elucidated key mechanisms within the complex regulatory network of T cell exhaustion. The critical role of Zbtb32 as a transcriptional activator and its interaction with factors like Bcl6 and Id2 offer new possibilities in improving diagnostic and therapeutic strategies in cancer immunotherapy.

Materials and methods

Mice

The research presented in this study has been conducted in accordance with all relevant ethical regulations. C57BL/6, CD45.1, *Tcrbd*$^{-/-}$, P14 (with transgenic expression of H-2D b-restricted TCR specific for gp33 epitope), and OT-I (with transgenic expression of H-2K b-restricted TCR specific for $OVA_{257–264}$) mice were originally obtained from the Jackson Laboratory (JAX: 030295). *Zbtb32*$^{-/-}$ mice were generated using standard CRISPR/Cas9 technology by truncating the second exon of Zbtb32, resulting in protein inactivation. The sequences of sgRNAs used in strain construction were gRNA1: 5′-CCAGAGTCAGTTAGGTTC TC-3′ and gRNA2: 5′-ACAAGCGAGTTGCAGAAGCCT-3′. The *CD8*^{Cre}*Bcl6*$^{fl/fl}$ mice were generated by crossing *CD8*^{Cre} and *Bcl6*$^{fl/fl}$ mice. *Zbtb32*$^{-/-}$ mice were crossed with *CD8*^{Cre}*Bcl6*$^{fl/fl}$ mice, and they were then crossed with P14 and OT-I mice. CD45.1 congenic mice were crossed with OT-I mice to generate CD45.1 OT-I mice. All the experiments were conducted using age- and sex-matched mice between the ages of 6 and 12 wk. The mice were maintained under specific pathogen–free conditions, and the animal protocols were approved by and performed in accordance with the Institutional Animal Care and Use Committee of Tsinghua University.

Flow cytometry and cell sorting

For surface marker detection, cells were incubated with the indicated antibodies against surface markers at 4°C for 30 min. For intracellular detection, cells were activated for 4 h with phorbol 12-myristate 13-acetate (PMA, 50 ng/ml; P8139; Sigma-Aldrich), ionomycin (500 ng/ml; I0634; Sigma-Aldrich), and Brefeldin A 596 (Golgiplug, BD Bioscience). Subsequently, the samples were fixed and permeabilized with a fixation/permeabilization kit (554722; BD Biosciences) according to the instructions from manufacturer.

Surface staining antibodies used included anti-Fixable Viability Dye (65-0866; eBioscience), anti-TCRβ (553172; BD Bioscience), anti-CD25 (25-0251-82; eBioscience), anti-TIM3 (25-0251-82; eBioscience), anti-CD45 (25-0451-81; eBioscience), anti-CD25 (25-0251-82; eBioscience), anti-CD3e (552774; BD Bioscience), anti-CD25 (25-0251-82; eBioscience), anti-Ly-6C (560593; BD Bioscience), anti-TCRβ (560657; BD Bioscience), anti-NK1.1 (45-5941-82; eBioscience), anti-CD8a (45-0081-82; eBioscience), anti-CD24 (101827; BioLegend), anti-CD44 (563058; BD Bioscience), anti-CD4 (100548; BioLegend), anti-F4/80 (123110; BioLegend), anti-CD69 (12-0691; eBioscience), anti-V alpha 2 TCR (12-5812; eBioscience), anti-CD11c (562454; BD Bioscience), anti-CD19 (562291; BD Bioscience), anti-γδTCR (553177; BD Bioscience), anti-CD45 (11-0541-82; eBioscience), anti-CD8a (11-0081-82; eBioscience), anti-CD3e (560801; BD Bioscience), anti-CD45R (560472; BD Bioscience), anti-CD127

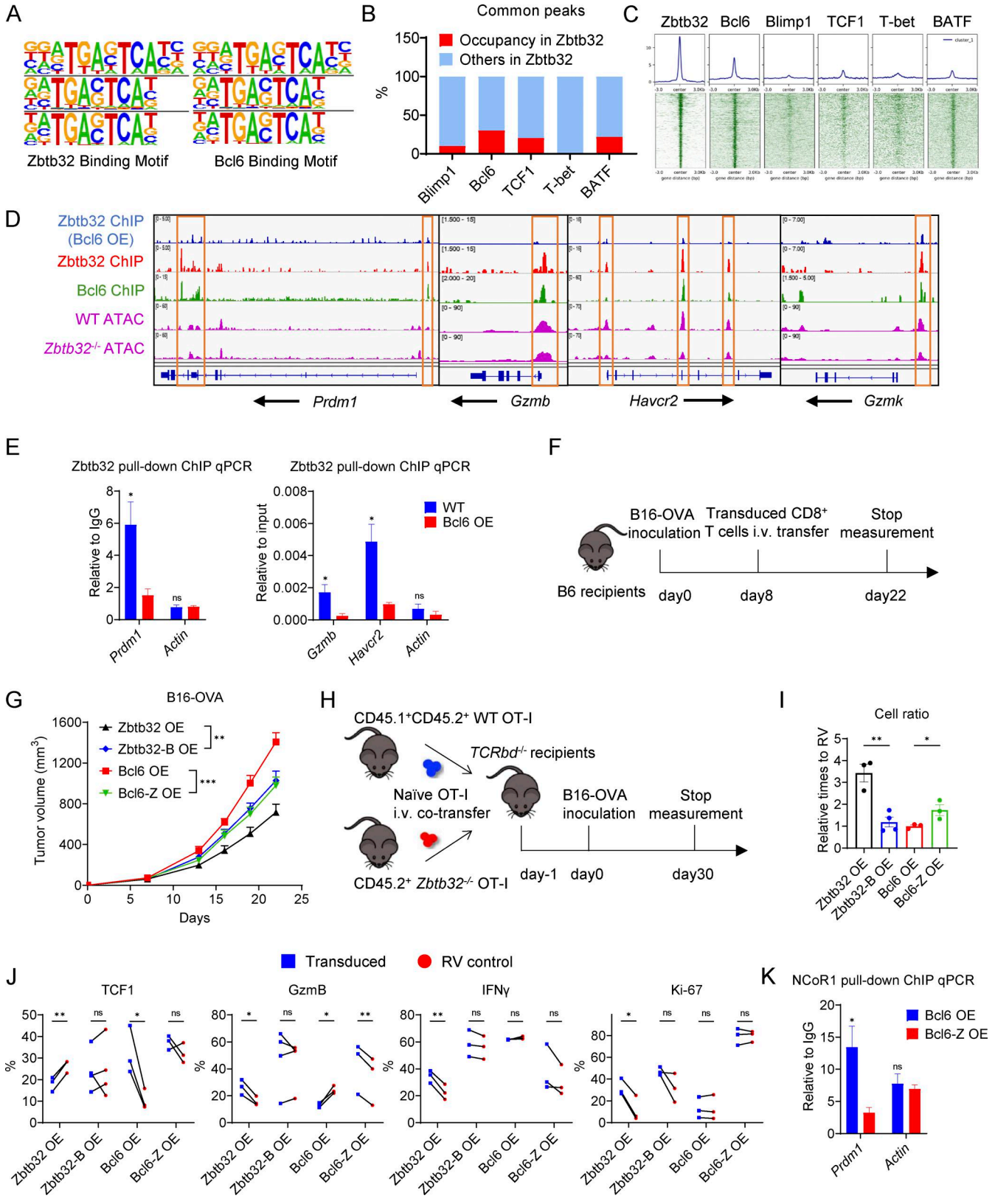

Figure 9. **Zbtb32 and Bcl6 exert antagonistic functions in tumor-specific CD8⁺ T cells. (A)** Consensus binding sequences of Zbtb32 and Bcl6. **(B)** Quantification of the ratios of ChIP-seq overlapped peaks bound by Zbtb32 and specific TFs in total Zbtb32-binding peaks in CD8⁺ T cells. **(C)** Heatmaps of read density profiles of Zbtb32 and other TFs ChIP-seq in CD8⁺ T cells surrounding Zbtb32-binding peaks, respectively. **(D)** Zbtb32, with or without Bcl6 overexpression, and Bcl6 occupancy at several classic gene loci were aligned with assay for ATAC-seq tracks of WT and *Zbtb32*$^{-/-}$ from B16-OVA tumor (GEO accession: GSE123236). The binding peaks on *Prdm1, Batf, Id2, Havcr2, Il2rb, Gzmb,* and *Gzmk* loci are shown. **(E)** ChIP-qPCR results showing the deposition of

Zbtb32 at specific gene loci in CD8⁺ T cells following 4-day activation *in vitro* with or without Bcl6 overexpression. The detected sites are labeled by blue arrow in Fig. S5 H (n = 3 for each group). **(F)** Schematic diagram of the transfer with 7 × 10^5 transduced OT-I cells on day 8. **(G)** The tumor growth in mice transferred with 0.7 × 10^6 activated CD8⁺ T cells with Zbtb32, Zbtb32-B, Bcl6, or Bcl6-Z overexpression on day 8 after inoculation with 1 × 10^6 B16-OVA cells (n = 6 for each group). **(H)** Schematic diagram of the co-transfer with 1.5×10^5 WT and 1.5 × 10^5 *Zbtb32*$^{-/-}$ naïve OT-I cells. **(I)** Quantifications of relative cell ratios in Zbtb32, Zbtb32-B, Bcl6, and Bcl6-Z OE activated CD8⁺ T cells in comparison with RV control CD8⁺ T cells, co-transferred into recipients on day 8 after 1 × 10^6 B16-OVA cells inoculation (n = 4 for each group). **(J)** Quantifications of specific molecules of transduced and RV control OT-I TILs in a co-transfer assay (n = 4 for each group). **(K)** ChIP-qPCR results demonstrating the deposition of NCoR1 at *Prdm1* gene locus in CD8⁺ T cells following 4-day activation *in vitro* with or without Bcl6 overexpression (n = 3 for each group). GEO accession: GSE182034. Data are shown as means ± SEM; ns, not significant; *P < 0.05, **P < 0.01, and ***P < 0.001 by paired (J) and unpaired (E, I, and K) two-tailed Student's t test and Bonferroni-corrected two-way ANOVA (G). Data shown are a representative (E, G, I, and J) or a pool (K) of two independent experiments. ATAC, transposase-accessible chromatin; Zbtb32-B, Zbtb32 with the Bcl6 BTB domain; Bcl6-Z, Bcl6 with the Zbtb32 BTB domain.

(48-1271-82; eBioscience), anti-Ly-6G (48-5931-82; eBioscience), anti-CD45.1 (48-4053-82; eBioscience), anti-CD8a (557959; BD Bioscience), anti-CD45.2 (56-0454; eBioscience), anti-CD62L (47-0621-82; eBioscience), anti-CD45.2 (109823; BioLegend), anti-MHCII (17-5321; eBioscience), anti-KLRG1 (561620; BD Bioscience), anti-CD3e (17-0032-82; eBioscience), anti-CD11b (17-0112-82; eBioscience), anti-Ly108 (12-1508-80, 17-1508-82; eBioscience).

Intracellular staining antibodies used included anti-Caspase-3 (561011; BD Bioscience), anti-KI-67 (556026; BD Bioscience), anti-KI-67 (556027; BD Bioscience), anti-IFNγ (554412; BD Bioscience), anti-IFNγ (48-7311-82; eBioscience), anti-IL-2 (560547; BD Bioscience), anti-IL-17A (11-7177-81; eBioscience), anti-TNFa (17-7321-82; eBioscience), anti-GzmB (50-8898-82; eBioscience), anti-Foxp3 (11-5773-82; eBioscience), anti-GATA3 (560074; BD Bioscience), anti-T-bet (25-5825-82; eBioscience), anti-TOX (50-6502-82; eBioscience), and anti-EOMES (48-4875-80; eBioscience).

For cell apoptosis analysis, the cells were fixed and incubated with PI from Annexin V Apoptosis Detection Kit I (556547; BD Bioscience) and Annexin V (550474; BD Bioscience) for 15 min at room temperature.

All cells were acquired using LSRFortessa (BD Bioscience) flow cytometer, and the data were analyzed using FlowJo V10.

CD8⁺ T cell purification and culture to induce exhaustion

CD8⁺ T cells were enriched from SPLs using Dynabeads FlowComp Mouse CD8 Kit (Invitrogen). Naïve CD8⁺ T cells were FACS sorted from CD8⁺CD25⁻CD44^{low}CD62L^{hi} population and cultured in RPMI 1640 medium supplemented with 10% (vol/vol) FBS (10099141C; Gibco), 1% (vol/vol) penicillin-streptomycin (30002-CI; Corning), 0.055 mM β-mercaptoethanol, 10 mM hepes (H4034; Sigma-Aldrich), and 1 mM sodium pyruvate (S6422; Gibco), 2 mM glutaMAX (35050061; Gibco) and activated with anti-CD3 (5 μg/ml, BE0001-1; BioXcell) plus anti-CD28 (1 μg/ml, BE0015-1; BioXcell) in the presence of 30 U/ml of IL-2 (212-12; PeproTech) *in vitro* for 6 days. The medium should be replenished with the same concentration of IL-2 every day after 3-day culture.

In vitro killing assay

Zbtb32$^{-/-}$ and WT OT-I naïve cells were activated with anti-CD3 (4 μg/ml, BE0001-1; BioXcell) and anti-CD28 (4 μg/ml, BE0015-1; BioXcell) antibodies *in vitro* for 48 h. Subsequently, live-activated OT-I cells were sorted and co-cultured with B16-OVA cells at different E:T ratios (4:1, 2:1, 1:1, 1:2, 1:4, and 1:10). B16-OVA tumor cells were pre-labeled with CellTrace Violet (C34557; Life Technologies), and analysis was conducted after a 12-h co-culture period.

Retrovirus packaging and infection

The CDS region of the genes was cloned into the digested vector to produce pRVKM-CDS-GFP plasmids. Plasmid transfection was performed when 293T cells reached 70–80% confluency. 12 μg pCL-Eco packaging plasmid, 12 μg pRVKM-CDS-GFP plasmid, and 93 μl 2M $CaCl_2$ were mixed in sterile water to reach a final volume of 750 μl. A volume of 750 μl of 2× HBS (pH 7.00) was added drop by drop while bubbling vigorously with an automatic pipette for 1 min, and HBS/DNA solution was then gently and quickly added drop wise onto medium, spreading across a 10-cm dish seeded with 293T cells. Lastly, 100 μM chloroquine was added to the dish and incubated at 37°C. Medium was changed 8 h later, and the supernatant containing virus particles was harvested 48 h after transfection. To obtain gene OE CD8⁺ T cells, naïve CD8⁺ T cells were cultured and activated with anti-CD3 (4 μg/ml) and anti-CD28 (4 μg/ml) *in vitro* for 48 h. The cells were infected with viral supernatants containing 2 μg/ml polybrene at 1,800 rpm. and 37°C for 1.5 h. Subsequently, the cells were then replenished with fresh medium and grown for 1–2 days. The infected cells were then sorted from activated GFP⁺ CD8⁺ T cells for subsequent assays.

Tumor inoculation and isolation of TILs

B16 and MC38 cells were cultured in DMEM, and E.G7 cells were cultured in RPMI 1640 medium, both supplemented with 10% FBS and 1% penicillin and streptomycin. A suspension of 5 × 10^5 B16, 1 × 10^6 E.G7, or 1 × 10^6 MC38 cells in 100 μl of 1× PBS was injected subcutaneously into 6–8-wk-old mice. Tumor growth was monitored every 2–3 days. Tumor volume was calculated by the following formula: tumor volume = length × width^2/2.

For isolation of TILs, all tumors were digested with 1 mg/ml of collagenase D supplemented with 10 U/ml of DNase I for 40 min at 37°C prior to centrifugation on a discontinuous Percoll gradient (GE Healthcare).

LM infection

Erythromycin-resistant LM-expressing $OVA_{257–264}$ were grown in brain heart infusion media supplemented with 5 μg/ml erythromycin. A suspension of 1 × 10^5 CFU of LM-OVA in 100 μl PBS was injected intravenously (i.v.) into 6–8-wk-old mice. The infected mice were analyzed on day 8 after injection.

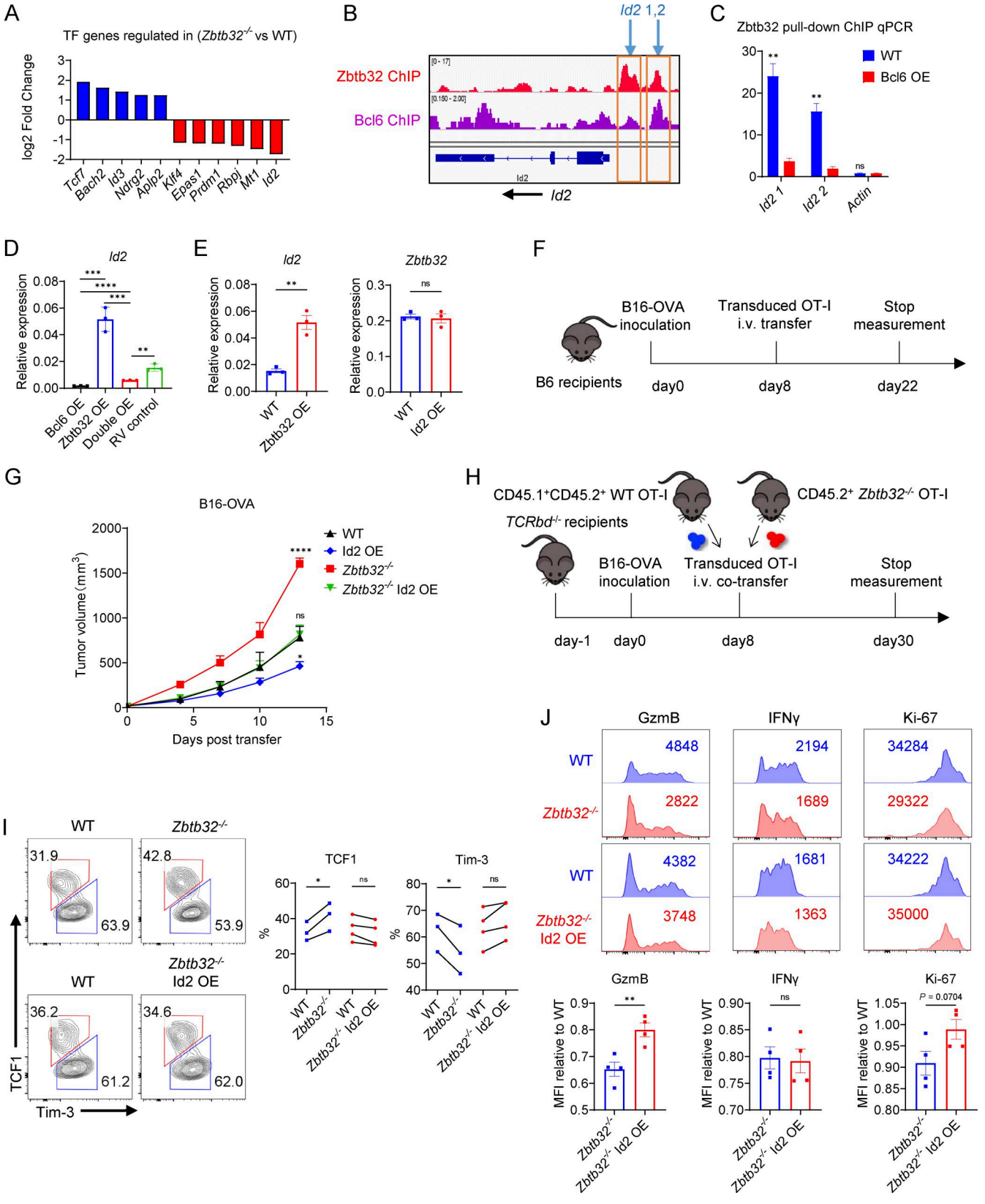

Figure 10. **Zbtb32 upregulates Id2 to enhance CD8⁺ T cell–mediated tumor rejection. (A)** Fold changes in the expression levels of different TFs in DEGs in *Zbtb32*$^{-/-}$ and WT CD8⁺ TILs. **(B)** The occupancies of Zbtb32 and Bcl6 at the *Id2* gene locus using ChIP-seq datasets. **(C)** ChIP-qPCR data showing the deposition of Zbtb32 at *Id2* locus in CD8⁺ T cells *in vitro* activated for 4 days with or without Bcl6 overexpression. The detected sites are labeled by blue arrows in Fig. 7 B (n = 3 for each group). **(D)** Quantifications of *Id2* expression in Bcl6-, Zbtb32-, double OE, and RV control activated CD8⁺ T cells measured by RT-qPCR (n = 3 for each group). **(E)** *Id2* expression in WT and Zbtb32 OE CD8⁺ T cells (left panel) and *Zbtb32* expression in WT and Id2 OE CD8⁺ T cells (right panel) measured by

RT-qPCR. **(F)** Schematic diagram of Id2 rescue assay in B6 mice, transferred with 7 × 10^5 transduced CD8$^+$ T cells on day 8 after inoculation of 1 × 10^6 B16-OVA cells. **(G)** Tumor growth in WT and *Zbtb32*$^{-/-}$ mice transferred with activated WT or *Zbtb32*$^{-/-}$ CD8$^+$ OT-I cells with or without Id2 overexpression (n = 6 for each group). **(H)** Schematic diagram of Id2 rescue assay in B6 mice, co-transferred with 5 × 10^5 transduced CD8$^+$ T cells on day 8 after inoculation of 1 × 10^6 B16-OVA cells. **(I)** Representative plots and quantifications of TCF1 and Tim-3 expressions in co-transferred WT and *Zbtb32*$^{-/-}$ CD8$^+$ TILs with or without Id2 overexpression (n = 4 for each group). **(J)** MFI and quantification of GzmB, IFNγ, and Ki-67 in WT and *Zbtb32*$^{-/-}$ CD8$^+$ OT-I TILs with or without Id2 overexpression (n = 4 for each group). Data are shown as means ± SEM; ns, not significant; *P < 0.05, **P < 0.01, ***P < 0.001, and ****P < 0.0001 by paired (I) and unpaired (C, D, E, and J) two-tailed Student's t test and Bonferroni-corrected two-way ANOVA (G). Data shown are a representative (C–J) of two independent experiments.

Bulk RNA-seq, ATAC-seq, and real-time qPCR

Naïve *Zbtb32*$^{-/-}$ and WT OT-I cells were sorted and co-transferred into CD45.1 mice one day before B16-OVA tumor cell inoculation. *Zbtb32*$^{-/-}$ and WT OT-I TILs were then sorted and prepared for RNA and ATAC sequencing.

Total RNA was extracted using TRIzol reagent (15596018; Invitrogen) according to the manufacturer's instructions and precipitated with isopropanol. The quantity and quality of the RNA were evaluated using the Agilent 2100 Bioanalyzer. The samples were sent to BGI Genomics for library construction and sequencing. Low-quality reads and adaptor sequences were removed using Trim Galore version 0.4.4. The clean reads were mapped to the *Mus musculus* genome (mm10) by Bowtie2 with default parameter. The identification of DEGs was based on a minimum 1.5-fold change.

For ATAC-seq analysis, the samples were resuspended in 35 µl of lysis buffer (10 mM Tris-HCl, pH 7.4, 10 mM NaCl, 3 mM $MgCl_2$, and 0.1% IGEPAL CA-630) and incubated on ice for 10 min with vortexing three times. Following addition of 10 µl of TruePrep Tagment Buffer L (TTBL) and 5 µl of TruePrep Tagment Enzyme (TTE) mix, the mixture was shaken at 37°C for 30 min to facilitate DNA fragmentation. The fragmented DNA was purified using 1.8-fold of AMPure beads, barcoded with dual indexes, and amplified by PCR. The DNA was then subjected to size selection and purification using 0.4-fold and 1.6-fold of AMPure beads, respectively. The size distribution and molarity of the library DNA were determined by Agilent 2100 bioanalyzer and Qubit. Sequencing was performed using Hiseq-PE150 (Illumina) provided by Novogene. Low-quality reads and adaptor sequences were removed by Trim Galore version 0.4.4 with parameters "-q 10-length 30-stringency 5". Paired-end reads were aligned to the mm10 reference genome using Bowtie2 with "-×2000". Reads that aligned to the mitochondrial genome were filtered, and PCR duplicates were removed with Picard MarkDuplicates. To identify peaks, the bam files containing unique, non-chrM reads were used to call peaks with MACS2 using parameters "–nomodel–keep-dup all -q 0.01–shift –100–extsize 200–call-summits -g mm." For differential coverage, corresponding bam files were merged to call peaks to get a union peak set. For each peak in the peak set, raw ATAC-seq reads were counted by featureCounts. Differentially expressed peaks were identified by at least twofold change and false discovery rate (FDR) adjusted P value of 0.01.

For real-time qPCR, M-MLV reverse transcription kit (Invitrogen) was used for generating cDNA. Gene expressions at the mRNA level were measured using the SYBR real-time kit (Bio-Rad Laboratories). For RT-qPCR analysis, the data shown were normalized to the expression of reference gene Actb. The primers used in RT-qPCR were as follows: *Zbtb32*-F: 5′-GGTGCTCCCTTCTCCCATAGT-3′, *Zbtb32*-R: 5′-GGAGTGGTTCAAGGTCAGTG-3′; *Gzmb*-F: 5′-TGTGAAGCCAGGAGATGTGT-3′, *Gzmb*-R: 5′-TCAGCTCAACCTCTTGTAGC-3′; *Ifng*-F: 5′-ACGGCACAGTCATTGAAAGC-3′, *Ifng*-R: 5′-GGCTCTGCAGGATTTTCATGTC-3′; *Bcl6*-F: 5′-CACACCCGTCCATCATT-GAA-3′, *Bcl6*-R: 5′-TGTCCTCACGGTGCCTTTTT-3′; *Tcf7*-F: 5′-AGCTTTCTCCACTCTA-CGAACA-3′, *Tcf7*-R: 5′-AATCCAGAGAGATCGGGGGTC-3′; *Havcr2*-F: 5′-ACAGAC-ACTGGTGACCCTCCAT-3′, *Havcr2*-R: 5′-CAGCAGAGACTCCCACTCCAAT-3′; *Il2ra*-F: 5′-AACCATAGTACCCAGTTGTCGG-3′, *Prdm1*-F: 5′-GACGGGGGTACTTCTGTTCA-3′, *Prdm1*-R: 5′-GGCATTCTTGGGAACTGTGT-3′; *Id2*-F: 5′-ATGAAAGCCTTCAGTCCGGTG-3′, *Id2*-R: 5′-AGCAGACTCATCGGGTCGT-3′; *Bach2*-F: 5′-AGATGACTTGGTGGTCAGCTTG-3′, *Bach2*-R: 5′-CTGCAAACAAACAGGCCATCCT-3′; and *Actb*-F: 5′-CCTGAACCCTAAG-GCCAAC-3′, *Actb*-R: 5′-ACAGCCTGGATGGCTACG-3′.

ChIP-seq and ChIP-qPCR

ChIP experiment was done following the manufacturer's instructions of Active Motif's ChIP assay kit (53035). 1 × 10^7 *in vitro*–cultured CD8$^+$ T cells were fixed by 1% paraformaldehyde, followed by digestion and sonication. All ChIP samples were collected from RV overexpression activated CD8$^+$ T cells, cultured *in vitro* for 4 days. The protocol was identical to that used for retrovirus infection.

The ChIP experiment was performed as indicated (Xu et al., 2019). The sequencing reads were mapped to the mouse genome mm 10 by Bowtie2 (Langmead and Salzberg, 2012). PCR duplicates were removed using Picard Mark Duplicates. The uniquely mapped reads were used to call peak with MACS2 using a P value cutoff of 0.01 (Zhang et al., 2008). ChIP seeker was used for peak annotation. deepTools was used to generate coverage track file (bigWig), which can be visualized in IGV 3. To generate a profile plot with deepTools (3.5.6), first use computeMatrix with parameters "–referencePoint center –missingDataAsZero -p 60 -R input.bed -S input.bw -b 5000 -a 5000 –skipZeros -o heatmap.gz" to calculate average signal values across regions. Signal normalization is typically applied during input file creation (using bamCoverage). Next, visualize with plotProfile using "-m (matrix file), –perGroup" to plot each group separately, and "–legendLocation" to position the legend. The y axis reflects the average signal intensity, depending on the chosen normalization method.

ChIP assay was performed using Active Motif's ChIP assay kit (53035) according to manufacturer's instructions with slight modifications (Wang et al., 2020). Briefly, a total of 1 × 10^7 cells were activated for 4 days and harvested and cross-linked with

paraformaldehyde. Then cells were lysed and digested with shearing enzyme followed by sonication. Anti-ZBTB32 antibody (ab235306; Abcam), Anti-HA-tag antibody (HA-Tag [C29F4] Rabbit mAb #3724; Cell Signaling), and Anti-NCoR antibody (A301-145A; Thermo Fisher Scientific) were added to supernatant followed by Dynabeads Protein A (Life Technologies) pulling down target fragment. The precipitated DNA was then washed, eluted, de-crosslinked, and purified for real-time qPCR analysis or sent to BGI Genomics for cDNA library preparation and sequencing. The following DNA fragments were amplified with primers as described: *Gzmb*-1-F: 5′-ATGACTGAGTTTGGGGTGAGGG-3′, *Gzmb*-1-R: 5′-GTG-AGTAAGCAACACCTTCCTT-3′; *Havcr2*-1-F: 5′-GTGTGTATGGC-TGCGTCATGCT-3′, *Havcr2*-1-R: 5′-CTACATGAGAGCATGCCTCAAA-3′; *Prdm1*-1-F: 5′-TTGGGCAGGTTCTCGCTAGCT-3′, *Prdm1*-1-R: 5′-ATGATGAAAGACTCTGAAGTCT-3′; *Id2*-1-F: 5′-TTCGCAGCCAATGCCTGTAGG-GT-3′, *Id2*-1-R: 5′-TAGCGACCTGTGACTTCCCGTCTG-3′; and *Id2*-2-F: 5′-TTGGAGCAA-CGCGGGAGGCCTT-3′, *Id2*-2-R: 5′-TAGTAACCCTGCCTCATTCTTGG-3′.

scRNA-seq analysis

scRNA-seq datasets were obtained from public resources GSE120575 (SKCM) and GSE122675 (B16) in the GEO database. Seurat (version 4.1) was used to perform dimensional reduction and clustering analysis of single-cell data. For dimensional reduction, t-distributed stochastic neighbor embedding (tSNE) was used for analysis. FindNeighbors and FindClusters function were used to cluster cells with a resolution of 1.0.

Statistical analysis

All statistical analysis was performed with Graph Prism 8.0.2 (GraphPad Prism software), and the results were presented as mean ± SEM. For two group comparisons, statistical analysis was performed using unpaired or paired two-tailed Student's *t* tests. Tumor growths were compared using Bonferroni-corrected two-way ANOVA. The log-rank (Mantel–Cox) test was employed to determine statistical significance of the survival of tumor-bearing mice and the survival of cancer patients from TCGA. Pearson r correlation values were calculated to evaluate the strength of the relationship between the expression patterns of individual genes or gene signatures. P values were calculated and presented in most of the data with *P < 0.05; **P < 0.01; ***P < 0.001; ****P < 0.0001.

Online supplemental material

Fig. S1 shows how *Zbtb32* enriched in T_{tex} CD8$^+$ TILs benefits clinical outcome. Fig. S2 shows how *Zbtb32* ablation worsens CD8$^+$ T cell anti-tumor capability. Fig. S3 shows how Zbtb32 exerts a long-term influence on CD8$^+$ T cells in tumor, but not in other immune organs. Fig. S4 shows how Zbtb32 transcriptionally regulates T_{tex} TIL function. Fig. S5 shows how Zbtb32 displays similar binding propensity but opposing regulation with Bcl6 in CD8$^+$ T cells.

Data availability

Data from ATAC-seq of WT and *Zbtb32*$^{-/-}$ OT-I cells co-transferred into B16-OVA–bearing mice in Fig. 8 and Fig. 9 D are available in the GEO database under accession no. GSE284603. Data from RNA-seq of WT and *Zbtb32*$^{-/-}$ OT-I cells co-transferred into B16-OVA–bearing mice in Fig. 7, D–H; Fig. 10 A; Fig. S4, D–F; and Fig. S5, C and D are available in the GEO database under accession no. GSE284604. ChIP-seq of Zbtb32 in CD8$^+$ T cells in Fig. 9, A–D; Fig. 10 B; and Fig. S5, A, B, D, and H are available in the GEO database under accession no. GSE284605.

Acknowledgments

We thank H. Qi from the Institute for Immunology at Tsinghua University in Beijing, China for providing *Zbtb32*$^{-/-}$ mice and X. Liu from South West Hospital at The Army Medical University in Chongqing, China for providing P14 mice. We thank the core facility of the Institute for Immunology at Tsinghua University for FACS sorting.

This work was supported by grants from the Natural Science Foundation of China (31991173 and 31991170), National Key Research and Development Program of China (2021YFC2302403), and Chinese Academy of Medical Sciences (CAMS) Innovation Fund for Medical Sciences (2022-I2M-5-01).

Author contributions: Birui Pan: conceptualization, data curation, formal analysis, investigation, project administration, software, supervision, validation, visualization, and writing—original draft, review, and editing. Qinli Sun: conceptualization, investigation, methodology, resources, and supervision. Ruifeng Li: data curation, visualization, and writing—original draft. Juan Feng: methodology. Jing Hao: resources. Bowen Xie: methodology and writing—review and editing. Xiaohong Zhao: data curation. Zixuan Zhao: resources. Peng Wei: methodology and resources. Qiuyan Lan: investigation and resources. Shiyuan Xie: formal analysis. Tian Xie: investigation. Yongzhen Chen: methodology. Kun Wei: resources. Xuan Zhong: validation. Hai Qi: resources. Ling Ni: formal analysis, supervision, and writing—original draft and writing—review and editing. Chen Dong: conceptualization, formal analysis, funding acquisition, project administration, and writing—original draft, review, and editing.

Disclosures: The authors declare no competing interests exist.

Submitted: 1 January 2025
Revised: 8 September 2025
Accepted: 17 December 2025

References

Adams, N.M., C.M. Lau, X. Fan, M. Rapp, C.D. Geary, O. El Weizman, C. Diaz-Salazar, and J.C. Sun. 2018. Transcription factor IRF8 orchestrates the adaptive natural killer cell response. *Immunity*. 48:1172–1182.e6. https://doi.org/10.1016/j.immuni.2018.04.018

Andrews, L.P., A.E. Marciscano, C.G. Drake, and D.A.A. Vignali. 2017. LAG3 (CD223) as a cancer immunotherapy target. *Immunol. Rev.* 276:80–96. https://doi.org/10.1111/imr.12519

Beaulieu, A.M., and D.B. Sant'Angelo. 2011. The BTB-ZF family of transcription factors: Key regulators of lineage commitment and effector function development in the immune system. *J. Immunol.* 187:2841–2847. https://doi.org/10.4049/jimmunol.1004006

Beaulieu, A.M., C.L. Zawislak, T. Nakayama, and J.C. Sun. 2014. The transcription factor Zbtb32 controls the proliferative burst of virus-specific

natural killer cells responding to infection. *Nat. Immunol.* 15:546–553. https://doi.org/10.1038/ni.2876

Brummelman, J., E.M.C. Mazza, G. Alvisi, F.S. Colombo, A. Grilli, J. Mikulak, D. Mavilio, M. Alloisio, F. Ferrari, E. Lopci, et al. 2018. High-dimensional single cell analysis identifies stemlike cytotoxic CD8+T cells infiltrating human tumors. *J. Exp. Med.* 215:2520–2535. https://doi.org/10.1084/JEM.20180684

Cannarile, M.A., N.A. Lind, R. Rivera, A.D. Sheridan, K.A. Camfield, B.B. Wu, K.P. Cheung, Z. Ding, and A.W. Goldrath. 2006. Transcriptional regulator Id2 mediates CD8+ T cell immunity. *Nat. Immunol.* 7:1317–1325. https://doi.org/10.1038/ni1403

Carmona, S.J., I. Siddiqui, M. Bilous, W. Held, and D. Gfeller. 2020. Deciphering the transcriptomic landscape of tumor-infiltrating CD8 lymphocytes in B16 melanoma tumors with single-cell RNA-Seq. *Oncoimmunology*. 9: 1737369. https://doi.org/10.1080/2162402X.2020.1737369

Chen, J., I.F. López-Moyado, H. Seo, C.W.J. Lio, L.J. Hempleman, T. Sekiya, A. Yoshimura, J.P. Scott-Browne, and A. Rao. 2019a. NR4A transcription factors limit CAR T cell function in solid tumours. *Nature*. 567:530–534. https://doi.org/10.1038/s41586-019-0985-x

Chen, Z., Z. Ji, S.F. Ngiow, S. Manne, Z. Cai, A.C. Huang, J. Johnson, R.P. Staupe, B. Bengsch, C. Xu, et al. 2019b. TCF-1-Centered transcriptional network drives an effector versus exhausted CD8 T cell-fate decision. *Immunity*. 51:840–855.e5. https://doi.org/10.1016/j.immuni.2019.09.013

Cheng, Z.Y., T.T. He, X.M. Gao, Y. Zhao, and J. Wang. 2021. ZBTB transcription factors: Key regulators of the development, differentiation and effector function of T cells. *Front. Immunol.* 12:713294. https://doi.org/10.3389/fimmu.2021.713294

Choi, J., and S. Crotty. 2021. Bcl6-Mediated transcriptional regulation of follicular helper T cells (TFH). *Trends Immunol.* 42:336–349. https://doi.org/10.1016/j.it.2021.02.002

Crotty, S. 2014. T follicular helper cell differentiation, function, and roles in disease. *Immunity*. 41:529–542. https://doi.org/10.1016/j.immuni.2014.10.004

Crotty, S., R.J. Johnston, and S.P. Schoenberger. 2010. Effectors and memories: Bcl-6 and Blimp-1 in T and B lymphocyte differentiation. *Nat. Immunol.* 11:114–120. https://doi.org/10.1038/ni.1837

Das, M., C. Zhu, and V.K. Kuchroo. 2017. Tim-3 and its role in regulating anti-tumor immunity. *Immunol. Rev.* 276:97–111. https://doi.org/10.1111/imr.12520

Dolina, J.S., N. Van Braeckel-Budimir, G.D. Thomas, and S. Salek-Ardakani. 2021. CD8+ T cell exhaustion in cancer. *Front. Immunol.* 12:715234. https://doi.org/10.3389/fimmu.2021.715234

Gebhardt, T., S.L. Park, and I.A. Parish. 2023. Stem-like exhausted and memory CD8+ T cells in cancer. *Nat. Rev. Cancer*. 23:780–798. https://doi.org/10.1038/s41568-023-00615-0

Hatzi, K., J. Philip Nance, M.A. Kroenke, M. Bothwell, E.K. Haddad, A. Melnick, and S. Crotty. 2015. BCL6 orchestrates Tfh cell differentiation via multiple distinct mechanisms. *J. Exp. Med.* 212:539–553. https://doi.org/10.1084/jem.20141380

Hoatlin, M.E., Z. Yu, H. Ball, K. Silvey, A. Melnick, S. Stone, S. Arai, N. Hawe, G. Owen, A. Zelent, and J.D. Licht. 1999. A novel BTB/POZ transcriptional repressor protein interacts with the Fanconi anemia group C protein and PLZF. *Blood*. 94:3737–3747. https://doi.org/10.1182/blood.v94.11.3737

Hoffmann, M.M., and J.E. Slansky. 2020. T-cell receptor affinity in the age of cancer immunotherapy. *Mol. Carcinog.* 59:862–870. https://doi.org/10.1002/mc.23212

Huang, Q., X. Wu, Z. Wang, X. Chen, L. Wang, Y. Lu, D. Xiong, Q. Liu, Y. Tian, H. Lin, et al. 2022. The primordial differentiation of tumor-specific memory CD8+ T cells as bona fide responders to PD-1/PD-L1 blockade in draining lymph nodes. *Cell*. 185:4049–4066.e25. https://doi.org/10.1016/j.cell.2022.09.020

Hudson, W.H., J. Gensheimer, M. Hashimoto, A. Wieland, R.M. Valanparambil, P. Li, J.X. Lin, B.T. Konieczny, S.J. Im, G.J. Freeman, et al. 2019. Proliferating transitory T cells with an effector-like transcriptional signature emerge from PD-1+ stem-like CD8+ T cells during chronic infection. *Immunity*. 51:1043–1058.e4. https://doi.org/10.1016/j.immuni.2019.11.002

Im, S.J., M. Hashimoto, M.Y. Gerner, J. Lee, H.T. Kissick, M.C. Burger, Q. Shan, J.S. Hale, J. Lee, T.H. Nasti, et al. 2016. Defining CD8+ T cells that provide the proliferative burst after PD-1 therapy. *Nature*. 537:417–421. https://doi.org/10.1038/nature19330

Jadhav, R.R., S.J. Im, B. Hu, M. Hashimoto, P. Li, J.X. Lin, W.J. Leonard, W.J. Greenleaf, R. Ahmed, and J.J. Goronzy. 2019. Epigenetic signature of PD-1+ TCF1+ CD8 T cells that act as resource cells during chronic viral infection and respond to PD-1 blockade. *Proc. Natl. Acad. Sci. USA*. 116: 14113–14118. https://doi.org/10.1073/pnas.1903520116

Jash, A., Y. Wang, F.J. Weisel, C.D. Scharer, J.M. Boss, M.J. Shlomchik, and D. Bhattacharya. 2016. ZBTB32 restricts the duration of memory B cell recall responses. *J. Immunol.* 197:1159–1168. https://doi.org/10.4049/jimmunol.1600882

Jin, Y., P. Hu, H. Sun, C. Yang, J. Zhai, Y. Wang, X. Chu, Z. Sun, J. Wang, J. Sun, and J. Wang. 2022. Expression of Id3 represses exhaustion of anti-tumor CD8 T cells in liver cancer. *Mol. Immunol.* 144:117–126. https://doi.org/10.1016/j.molimm.2022.02.005

Johnston, R.J., A.C. Poholek, D. DiToro, I. Yusuf, D. Eto, B. Barnett, A.L. Dent, J. Craft, and S. Crotty. 2009. Bcl6 and Blimp-1 are reciprocal and antagonistic regulators of T follicular helper cell differentiation. *Science*. 325: 1006–1010. https://doi.org/10.1126/science.1175870

Jung, I.Y., V. Narayan, S. McDonald, A.J. Rech, R. Bartoszek, G. Hong, M.M. Davis, J. Xu, A.C. Boesteanu, J.S. Barber-Rotenberg, et al. 2022. BLIMP1 and NR4A3 transcription factors reciprocally regulate antitumor CAR T cell stemness and exhaustion. *Sci. Transl. Med.* 14:eabn7336. https://doi.org/10.1126/scitranslmed.abn7336

Kelly, K.F., and J.M. Daniel. 2006. POZ for effect - POZ-ZF transcription factors in cancer and development. *Trends Cell Biol.* 16:578–587. https://doi.org/10.1016/j.tcb.2006.09.003

Khan, O., J.R. Giles, S. McDonald, S. Manne, S.F. Ngiow, K.P. Patel, M.T. Werner, A.C. Huang, K.A. Alexander, J.E. Wu, et al. 2019. TOX transcriptionally and epigenetically programs CD8+ T cell exhaustion. *Nature*. 571:211–218. https://doi.org/10.1038/s41586-019-1325-x

Kim, K., S. Park, S.Y. Park, G. Kim, S.M. Park, J.W. Cho, D.H. Kim, Y.M. Park, Y.W. Koh, H.R. Kim, et al. 2020. Single-cell transcriptome analysis reveals TOX as a promoting factor for T cell exhaustion and a predictor for anti-PD-1 responses in human cancer. *Genome Med.* 12:22. https://doi.org/10.1186/s13073-020-00722-9

Kurtulus, S., A. Madi, G. Escobar, M. Klapholz, J. Nyman, E. Christian, M. Pawlak, D. Dionne, J. Xia, O. Rozenblatt-Rosen, et al. 2019. Checkpoint blockade immunotherapy induces dynamic changes in PD-1 – CD8 + tumor-infiltrating T cells. *Immunity*. 50:181–194.e6. https://doi.org/10.1016/j.immuni.2018.11.014

Lagumdzic, E., C. Pernold, M. Viano, S. Olgiati, M.W. Schmitt, K.H. Mair, and A. Saalmüller. 2022. Transcriptome profiling of porcine naïve, intermediate and terminally differentiated CD8+ T cells. *Front. Immunol.* 13: 849922. https://doi.org/10.3389/fimmu.2022.849922

Langmead, B., and S.L. Salzberg. 2012. Fast gapped-read alignment with Bowtie 2. *Nat. Methods*. 9:357–359. https://doi.org/10.1038/nmeth.1923

Li, Y., M. Han, H. Wei, W. Huang, Z. Chen, T. Zhang, M. Qian, L. Jing, G. Nan, X. Sun, et al. 2024. Id2 epigenetically controls CD8+ T-cell exhaustion by disrupting the assembly of the Tcf3-LSD1 complex. *Cell. Mol. Immunol.* 21:292–308. https://doi.org/10.1038/s41423-023-01118-6

Liu, B., X. Hu, K. Feng, R. Gao, Z. Xue, S. Zhang, Y. Zhang, E. Corse, Y. Hu, W. Han, and Z. Zhang. 2022. Temporal single-cell tracing reveals clonal revival and expansion of precursor exhausted T cells during anti-PD-1 therapy in lung cancer. *Nat. Cancer*. 3:108–121. https://doi.org/10.1038/s43018-021-00292-8

Liu, X., R.I. Nurieva, and C. Dong. 2013. Transcriptional regulation of follicular T-helper (Tfh) cells. *Immunol. Rev.* 252:139–145. https://doi.org/10.1111/imr.12040

McLane, L.M., M.S. Abdel-Hakeem, and E.J. Wherry. 2019. CD8 T cell exhaustion during chronic viral infection and cancer. *Annu. Rev. Immunol.* 37:457–495. https://doi.org/10.1146/annurev-immunol-041015-055318

McMahan, R.H., J.A. McWilliams, K.R. Jordan, S.W. Dow, D.B. Wilson, and J.E. Slansky. 2006. Relating TCR-peptide-MHC affinity to immunogenicity for the design of tumor vaccines. *J. Clin. Invest.* 116:2543–2551. https://doi.org/10.1172/JCI26936

Miaw, S.C., A. Choi, E. Yu, H. Kishikawa, and I.C. Ho. 2000. ROG, repressor of GATA, regulates the expression of cytokine genes. *Immunity*. 12: 323–333. https://doi.org/10.1016/S1074-7613(00)80185-5

Miller, B.C., D.R. Sen, R. Al Abosy, K. Bi, Y.V. Virkud, M.W. LaFleur, K.B. Yates, A. Lako, K. Felt, G.S. Naik, et al. 2019. Subsets of exhausted CD8+ T cells differentially mediate tumor control and respond to checkpoint blockade. *Nat. Immunol.* 20:326–336. https://doi.org/10.1038/s41590-019-0312-6

Mognol, G.P., R. Spreafico, V. Wong, J.P. Scott-Browne, S. Togher, A. Hoffmann, P.G. Hogan, A. Rao, and S. Trifari. 2017. Exhaustion-associated regulatory regions in CD8+ tumor-infiltrating T cells. *Proc. Natl. Acad. Sci. USA*. 114:E2776–E2785. https://doi.org/10.1073/pnas.1620498114

Mondal, A., D. Sawant, and A.L. Dent. 2010. Transcriptional repressor BCL6 controls Th17 responses by controlling gene expression in both T cells and macrophages. *J. Immunol.* 184:4123–4132. https://doi.org/10.4049/jimmunol.0901242

Niu, H., and H. Wang. 2023. TOX regulates T lymphocytes differentiation and its function in tumor. *Front. Immunol.* 14:990419. https://doi.org/10.3389/fimmu.2023.990419

Nurieva, R.I., Y. Chung, G.J. Martinez, X.O. Yang, S. Tanaka, T.D. Matskevitch, Y.H. Wang, and C. Dong. 2009. Bcl6 mediates the development of T follicular helper cells. *Science*. 325:1001–1005. https://doi.org/10.1126/science.1176676

Omilusik, K.D., M.S. Nadjsombati, L.A. Shaw, B. Yu, J. Justin Milner, and A.W. Goldrath. 2018. Sustained Id2 regulation of E proteins is required for terminal differentiation of effector CD8 + T cells. *J. Exp. Med.* 215:773–783. https://doi.org/10.1084/jem.20171584

Omori, M., M. Yamashita, M. Inami, M. Ukai-Tadenuma, M. Kimura, Y. Nigo, H. Hosokawa, A. Hasegawa, M. Taniguchi, and T. Nakayama. 2003. CD8 T cell-specific downregulation of histone hyperacetylation and gene activation of the IL-4 gene locus by ROG, repressor of GATA. *Immunity*. 19:281–294. https://doi.org/10.1016/S1074-7613(03)00210-3

Paley, M.A., D.C. Kroy, P.M. Odorizzi, J.B. Johnnidis, D.V. Dolfi, B.E. Barnett, E.K. Bikoff, E.J. Robertson, G.M. Lauer, S.L. Reiner, and E.J. Wherry. 2012. Progenitor and terminal subsets of CD8+ T cells cooperate to contain chronic viral infection. *Science*. 80:1220–1225. https://doi.org/10.1126/science.1229620

Philip, M., and A. Schietinger. 2022. CD8+ T cell differentiation and dysfunction in cancer. *Nat. Rev. Immunol.* 22:209–223. https://doi.org/10.1038/s41577-021-00574-3

Piazza, F., J.A. Costoya, T. Merghoub, R.M. Hobbs, and P.P. Pandolfi. 2004. Disruption of PLZP in mice leads to increased T-lymphocyte proliferation, cytokine production, and altered hematopoietic stem cell homeostasis. *Mol. Cell. Biol.* 24:10456–10469. https://doi.org/10.1128/mcb.24.23.10456-10469.2004

Ribas, A., and J.D. Wolchok. 2018. Cancer immunotherapy using checkpoint blockade. *Science*. 359:1350–1355. https://doi.org/10.1126/science.aar4060

Schietinger, A., and P.D. Greenberg. 2014. Tolerance and exhaustion: Defining mechanisms of T cell dysfunction. *Trends Immunol.* 35:51–60. https://doi.org/10.1016/j.it.2013.10.001

Scott, A.C., F. Dündar, P. Zumbo, S.S. Chandran, C.A. Klebanoff, M. Shakiba, P. Trivedi, L. Menocal, H. Appleby, S. Camara, et al. 2019. TOX is a critical regulator of tumour-specific T cell differentiation. *Nature*. 571:270–274. https://doi.org/10.1038/s41586-019-1324-y

Seo, H., J. Chen, E. González-Avalos, D. Samaniego-Castruita, A. Das, Y.H. Wang, I.F. López-Moyado, R.O. Georges, W. Zhang, A. Onodera, et al. 2019. TOX and TOX2 transcription factors cooperate with NR4A transcription factors to impose CD8+ T cell exhaustion. *Proc. Natl. Acad. Sci. USA*. 116:12410–12415. https://doi.org/10.1073/pnas.1905675116

Seo, H., E. González-Avalos, W. Zhang, P. Ramchandani, C. Yang, C.W.J. Lio, A. Rao, and P.G. Hogan. 2021. BATF and IRF4 cooperate to counter exhaustion in tumor-infiltrating CAR T cells. *Nat. Immunol.* 22:983–995. https://doi.org/10.1038/s41590-021-00964-8

Shin, H., S.D. Blackburn, A.M. Intlekofer, C. Kao, J.M. Angelosanto, S.L. Reiner, and E.J. Wherry. 2009. A role for the transcriptional repressor blimp-1 in CD8+ T cell exhaustion during chronic viral infection. *Immunity*. 31:309–320. https://doi.org/10.1016/j.immuni.2009.06.019

Shin, H.M., V.N. Kapoor, G. Kim, P. Li, H.R. Kim, M. Suresh, S.M. Kaech, E.J. Wherry, L.K. Selin, W.J. Leonard, et al. 2017. Transient expression of ZBTB32 in anti-viral CD8+T cells limits the magnitude of the effector response and the generation of memory. *PLoS Pathog.* 13:e1006544. https://doi.org/10.1371/journal.ppat.1006544

Sun, Q., D. Cai, D. Liu, X. Zhao, R. Li, W. Xu, B. Xie, M. Gou, K. Wei, Y. Li, et al. 2023a. BCL6 promotes a stem-like CD8+ T cell program in cancer via antagonizing BLIMP1. *Sci. Immunol.* 8:eadh1306. https://doi.org/10.1126/sciimmunol.adh1306

Sun, Q., X. Zhao, R. Li, D. Liu, B. Pan, B. Xie, X. Chi, D. Cai, P. Wei, W. Xu, et al. 2023b. STAT3 regulates CD8+ T cell differentiation and functions in cancer and acute infection. *J. Exp. Med.* 220:e20220686. https://doi.org/10.1084/jem.20220686

Tillé, L., D. Cropp, M. Charmoy, P. Reichenbach, M. Andreatta, T. Wyss, G. Bodley, I. Crespo, S. Nassiri, J. Lourenco, et al. 2023. Activation of the transcription factor NFAT5 in the tumor microenvironment enforces CD8+ T cell exhaustion. *Nat. Immunol.* 24:1645–1653. https://doi.org/10.1038/s41590-023-01614-x

Utzschneider, D.T., M. Charmoy, V. Chennupati, L. Pousse, D.P. Ferreira, S. Calderon-Copete, M. Danilo, F. Alfei, M. Hofmann, D. Wieland, et al. 2016. T cell factor 1-expressing memory-like CD8+ T cells sustain the immune response to chronic viral infections. *Immunity*. 45:415–427. https://doi.org/10.1016/j.immuni.2016.07.021

Vasanwala, F.H., S. Kusam, L.M. Toney, and A.L. Dent. 2002. Repression of AP-1 function: A mechanism for the regulation of blimp-1 expression and B lymphocyte differentiation by the B cell lymphoma-6 protooncogene. *J. Immunol.* 169:1922–1929. https://doi.org/10.4049/jimmunol.169.4.1922

Wang, X., L. Ni, S. Wan, X. Zhao, X. Ding, A. Dejean, and C. Dong. 2020. Febrile temperature critically controls the differentiation and pathogenicity of T helper 17 cells. *Immunity*. 52:328–341.e5. https://doi.org/10.1016/j.immuni.2020.01.006

Wei, S.C., J.H. Levine, A.P. Cogdill, Y. Zhao, N.A.A.S. Anang, M.C. Andrews, P. Sharma, J. Wang, J.A. Wargo, D. Pe'er, and J.P. Allison. 2017. Distinct cellular mechanisms underlie anti-CTLA-4 and anti-PD-1 checkpoint blockade. *Cell*. 170:1120–1133.e17. https://doi.org/10.1016/j.cell.2017.07.024

Wherry, E.J., S.J. Ha, S.M. Kaech, W.N. Haining, S. Sarkar, V. Kalia, S. Subramaniam, J.N. Blattman, D.L. Barber, and R. Ahmed. 2007. Molecular signature of CD8+ T cell exhaustion during chronic viral infection. *Immunity*. 27:670–684. https://doi.org/10.1016/j.immuni.2007.09.006

Wherry, E.J., and M. Kurachi. 2015. Molecular and cellular insights into T cell exhaustion. *Nat. Rev. Immunol.* 15:486–499. https://doi.org/10.1038/nri3862

Wu, T., Y. Ji, E. Ashley Moseman, H.C. Xu, M. Manglani, M. Kirby, S.M. Anderson, R. Handon, E. Kenyon, A. Elkahloun, et al. 2016. The TCF1-Bcl6 axis counteracts type I interferon to repress exhaustion and maintain T cell stemness. *Sci. Immunol.* 1:eaai8593. https://doi.org/10.1126/sciimmunol.aai8593

Xu, W., X. Zhao, X. Wang, H. Feng, M. Gou, W. Jin, X. Wang, X. Liu, and C. Dong. 2019. The transcription factor Tox2 drives T follicular helper cell development via regulating chromatin accessibility. *Immunity*. 51:826–839.e5. https://doi.org/10.1016/j.immuni.2019.10.006

Yang, C.Y., J.A. Best, J. Knell, E. Yang, A.D. Sheridan, A.K. Jesionek, H.S. Li, R.R. Rivera, K.C. Lind, L.M. D'Cruz, et al. 2011. The transcriptional regulators Id2 and Id3 control the formation of distinct memory CD8 + T cell subsets. *Nat. Immunol.* 12:1221–1229. https://doi.org/10.1038/ni.2158

Yang, M., Q. Huang, C. Li, Z. Jiang, J. Sun, Z. Wang, R. Liang, D. Li, B. Li, and H. Zhao. 2021. TOX acts as a tumor suppressor by inhibiting mTOR signaling in colorectal cancer. *Front. Immunol.* 12:647540. https://doi.org/10.3389/fimmu.2021.647540

Yao, C., G. Lou, H.W. Sun, Z. Zhu, Y. Sun, Z. Chen, D. Chauss, E.A. Moseman, J. Cheng, M.A. D'Antonio, et al. 2021. BACH2 enforces the transcriptional and epigenetic programs of stem-like CD8+ T cells. *Nat. Immunol.* 22:370–380. https://doi.org/10.1038/s41590-021-00868-7

Yoon, H.S., C.D. Scharer, P. Majumder, C.W. Davis, R. Butler, W. Zinzow-Kramer, I. Skountzou, D.G. Koutsonanos, R. Ahmed, and J.M. Boss. 2012. ZBTB32 is an early repressor of the CIITA and MHC class II gene expression during B cell differentiation to plasma cells. *J. Immunol.* 189:2393–2403. https://doi.org/10.4049/jimmunol.1103371

Zajac, A.J., J.N. Blattman, K. Murali-Krishna, D.J.D. Sourdive, M. Suresh, J.D. Altman, and R. Ahmed. 1998. Viral immune evasion due to persistence of activated T cells without effector function. *J. Exp. Med.* 188:2205–2213. https://doi.org/10.1084/jem.188.12.2205

Zhang, Y., T. Liu, C.A. Meyer, J. Eeckhoute, D.S. Johnson, B.E. Bernstein, C. Nussbaum, R.M. Myers, M. Brown, W. Li, and X.S. Shirley. 2008. Model-based analysis of ChIP-seq (MACS). *Genome Biol.* 9:R137. https://doi.org/10.1186/gb-2008-9-9-r137

Zook, E.C., Z.Y. Li, Y. Xu, R.F. de Pooter, M. Verykokakis, A. Beaulieu, A. Lasorella, M. Maienschein-Cline, J.C. Sun, M. Sigvardsson, and B.L. Kee. 2018. Transcription factor ID2 prevents E proteins from enforcing a naïve T lymphocyte gene program during NK cell development. *Sci. Immunol.* 3:eaao2139. https://doi.org/10.1126/sciimmunol.aao2139

Supplemental material

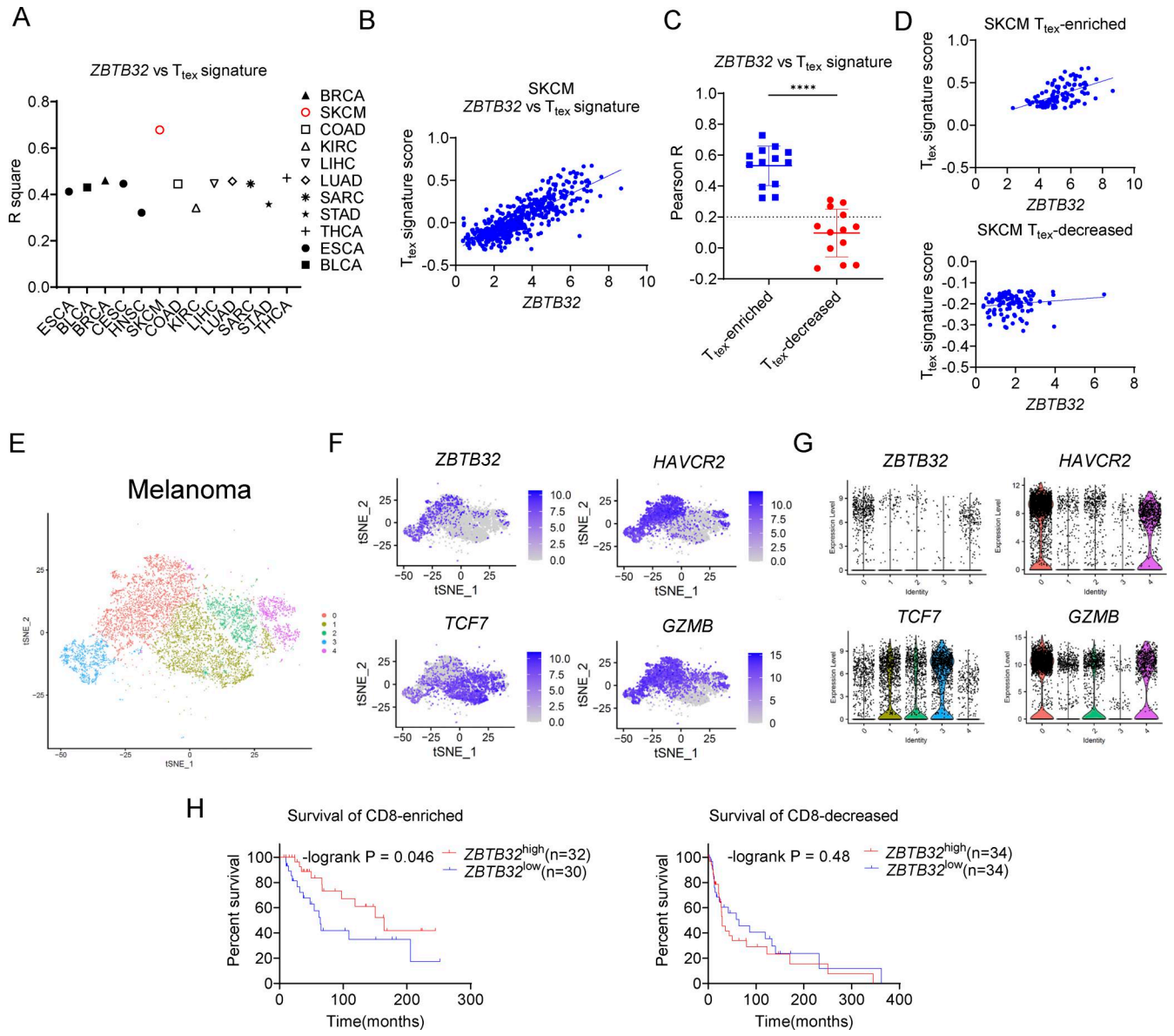

Figure S1. ***Zbtb32* enriched in T_{tex} CD8⁺ TILs benefits clinical outcome. (A)** Correlations between *ZBTB32* expression and T_{tex} signature score in diverse cancer patients. **(B)** Correlation between *ZBTB32* expression and T_{tex} signature score in SKCM patients. **(C)** Correlations between *ZBTB32* expression and T_{tex} signature score in T_{tex} signature-enriched (blue) and -decreased groups (red) of diverse cancer patients. **(D)** Correlations of *ZBTB32* expression versus T_{tex} signature score in T_{tex} signature-enriched and -decreased groups of SKCM patients. **(E)** The tSNE plot of scRNA-seq dataset indicating global transcriptomic similarities of CD8⁺ TILs in SKCM TME. **(F)** FeaturePlots showing expression profiles of *ZBTB32* and other classic genes in SKCM CD8⁺ TILs. **(G)** The expression levels of *ZBTB32* and other classic genes in the different clusters of SKCM CD8⁺ TILs. **(H)** The overall survival rates for $ZBTB32^{high}$ and $ZBTB32^{low}$ SKCM patients with enriched or decreased CD8⁺ TILs. GEO accessions: (A) and B) GSE182035, (E–G) GSE120575. R square (A), Pearson R (B, C, and D), unpaired two-tailed Student's *t* test (C), and Mantel–Cox test (H); ****P < 0.0001.

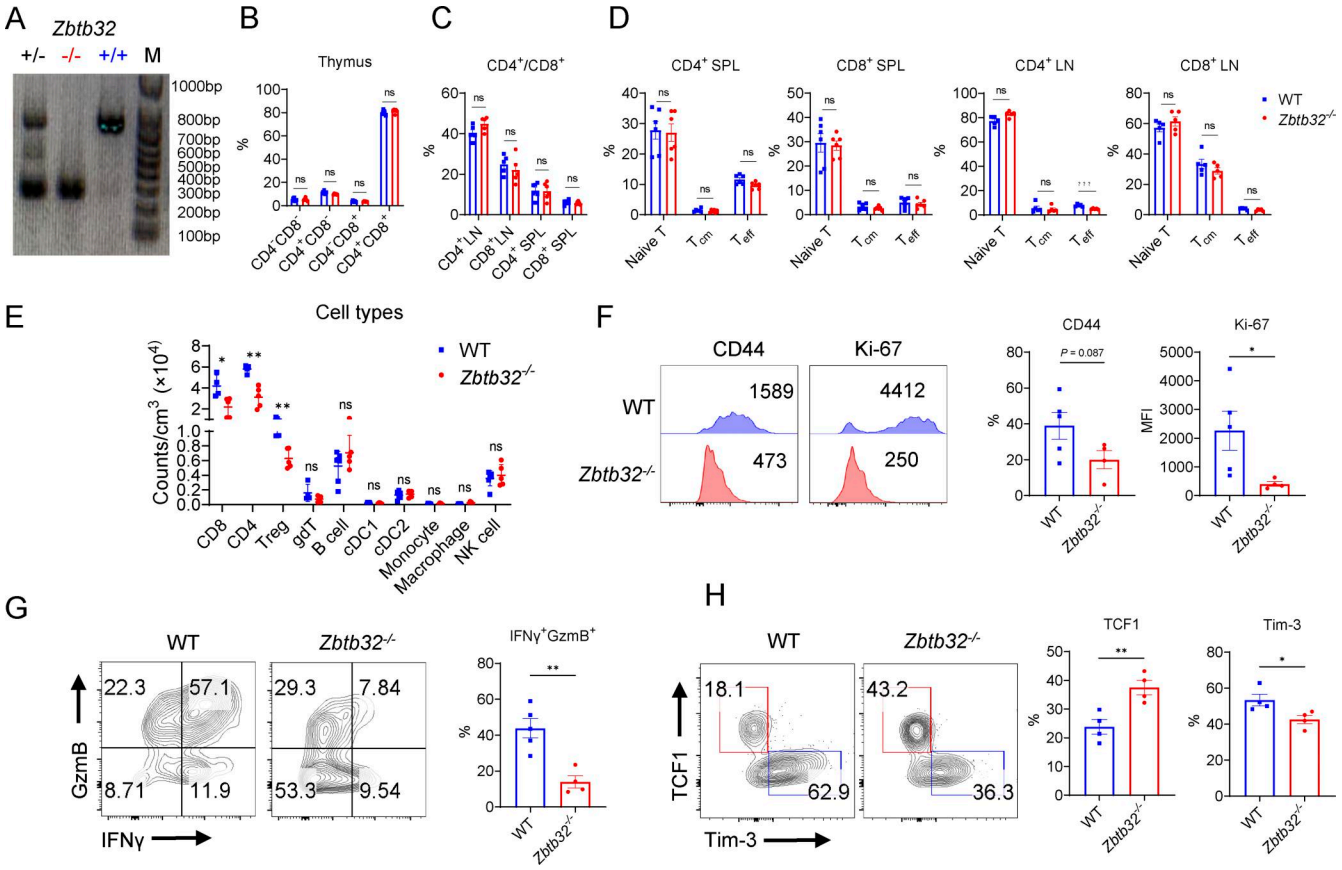

Figure S2. ***Zbtb32* ablation worsens CD8⁺ T cell anti-tumor capability. (A)** Characterization of *Zbtb32*$^{-/-}$ mice. **(B)** Quantification of CD4⁺/CD8⁺ cell ratio in thymus in WT and *Zbtb32*$^{-/-}$ mice (n = 6 for each group). **(C)** Quantification of CD4⁺/CD8⁺ T cell ratio in SPL and LN in WT and *Zbtb32*$^{-/-}$ mice (n = 6 for each group). **(D)** Quantification of different subsets of CD4⁺/CD8⁺ cells in SPL and LN in WT and *Zbtb32*$^{-/-}$ mice (n = 6 for each group). **(E)** Quantification of cell counts of different immune cell types in WT and *Zbtb32*$^{-/-}$ CD8⁺ TILs in B16-OVA TME (n = 5 for each group). **(F)** MFI and quantification of CD44 and Ki-67 in WT and *Zbtb32*$^{-/-}$ CD8⁺ TILs in B16-OVA TME (n = 5 for each group). **(G)** Representative plots and quantification of IFNγ, GzmB, and CD8⁺/CD4⁺ ratio in WT and *Zbtb32*$^{-/-}$ CD8⁺ TILs in B16-OVA TME. **(H)** Representative FACS plots (left panel) and quantification (right panel) of TCF1 and Tim-3 in WT and *Zbtb32*$^{-/-}$ CD8⁺ TILs in B16-OVA TME (n = 5 for each group). Data are all shown as means ± SEM; ns, not significant; *P < 0.05 and **P < 0.01 by unpaired two-tailed Student's t test. Data shown in all graphs are a representative of two independent experiments. Source data are available for this figure: SourceData FS2.

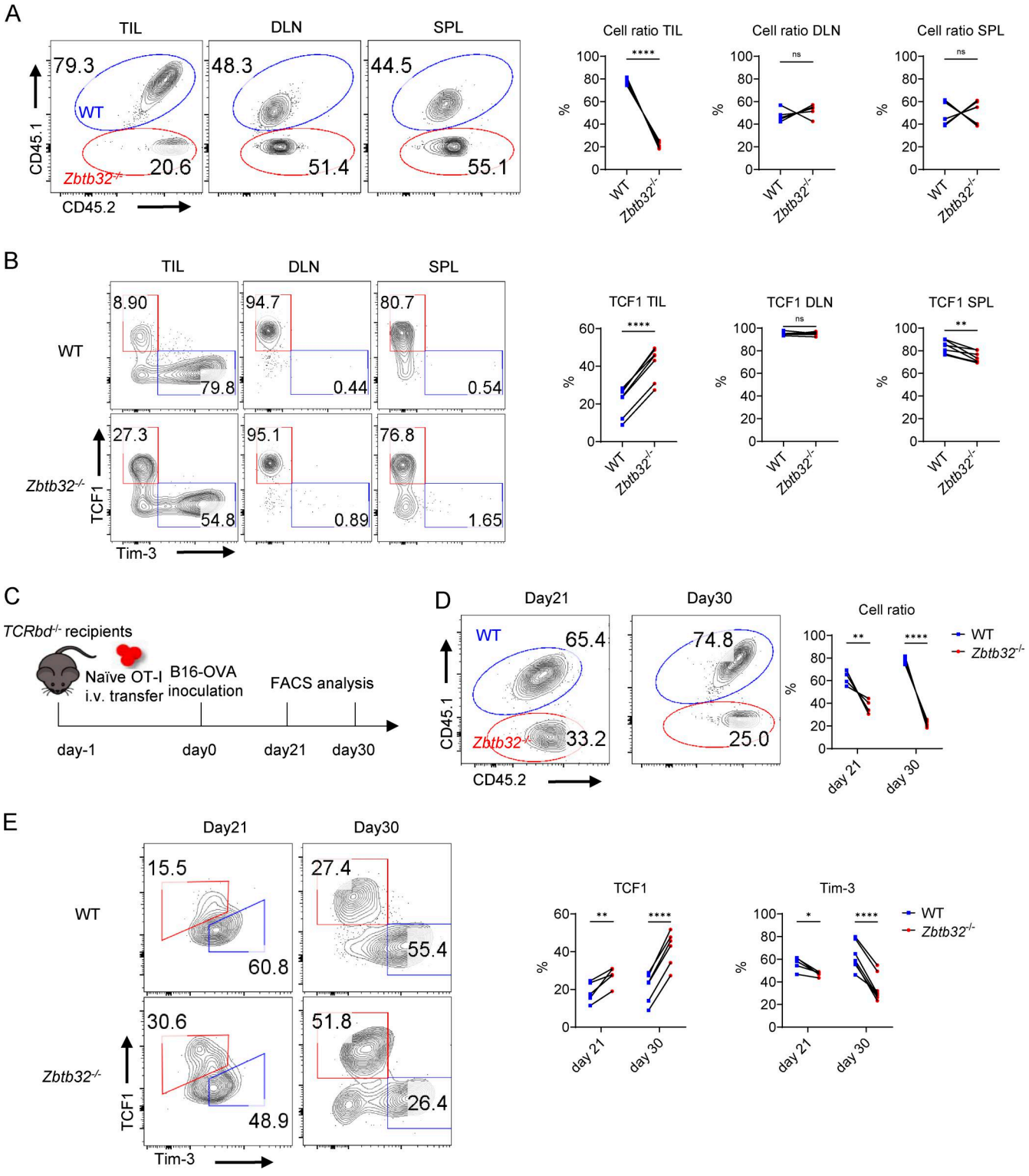

Figure S3. **Zbtb32 exerts a long-term influence on CD8⁺ T cells in tumor, but not in other immune organs. (A)** Representative plots and quantifications of WT and *Zbtb32*$^{-/-}$ OT-I cells in TILs, DLN, and SPL (n = 5 in each group). **(B)** Representative plots (left panel) and quantifications (right panel) of TCF1 and Tim-3 in WT and *Zbtb32*$^{-/-}$ OT-I cells in TILs, DLN, and SPL (n = 5 in each group). **(C)** Schematic diagram of the co-transfer of 1.5 × 10^5 WT and 1.5 × 10^5 *Zbtb32*$^{-/-}$ naïve OT-I cells before 1 × 10^6 B16-OVA inoculation and collection at early and late time points (n = 5 in each group). **(D)** Representative plots and quantifications of WT and *Zbtb32*$^{-/-}$ OT-I cells in TILs at different time points (n = 5 in each group). **(E)** Representative plots (left panel) and quantifications (right panel) of TCF1 and Tim-3 in WT and *Zbtb32*$^{-/-}$ OT-I cells in TILs at different time points (n = 5 in each group). Data in all graphs are shown as means ± SEM; ns, not significant; *P < 0.05, **P < 0.01 and ****P < 0.0001 by paired two-tailed Student's t test. Data shown are a representative of two independent experiments.

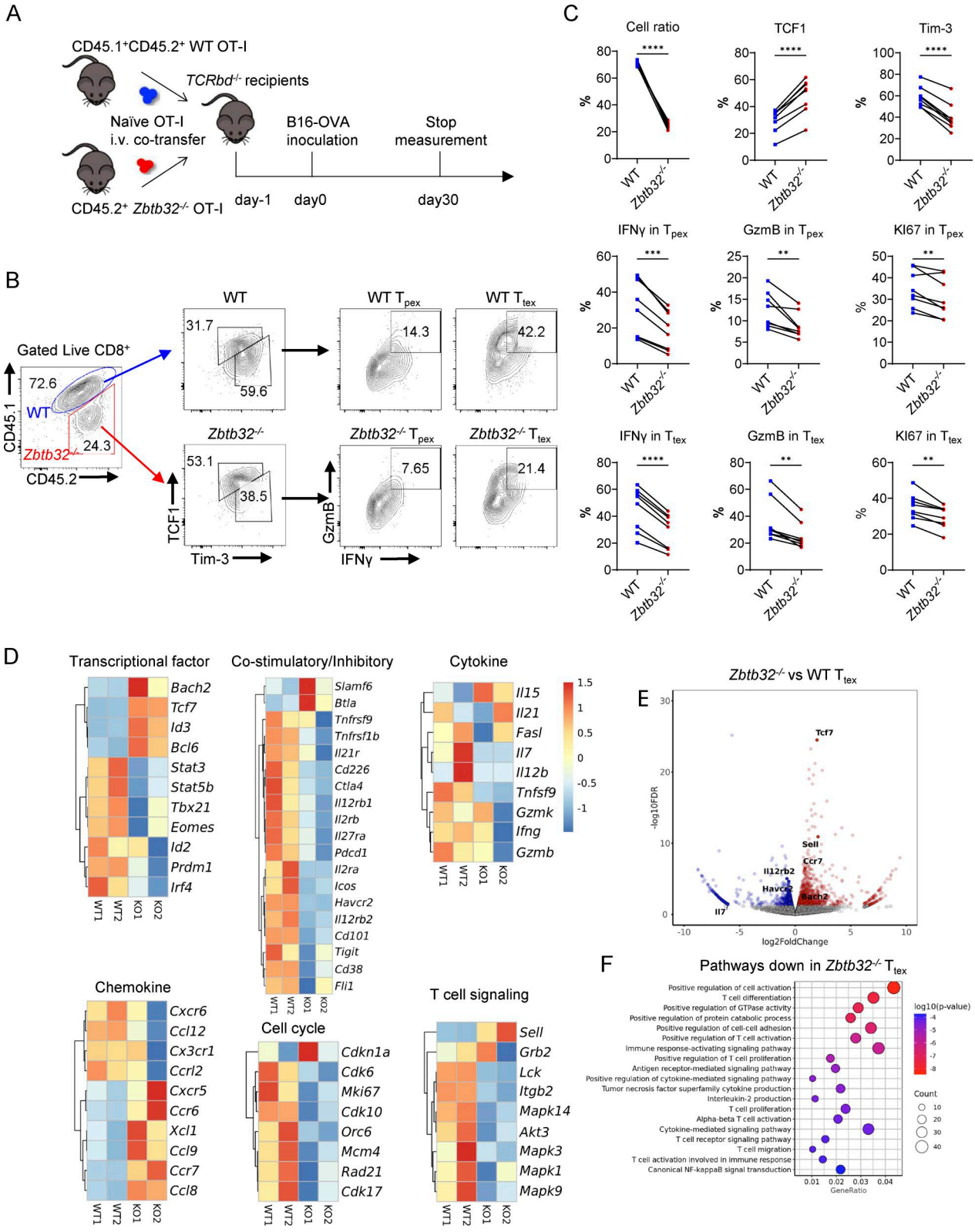

Figure S4. **Zbtb32 transcriptionally regulates T_{ex} TIL function. (A)** Schematic diagram of the co-transfer of 1.5×10^5 WT and 1.5×10^5 *Zbtb32*$^{-/-}$ naïve OT-I cells prior to 1×10^6 B16-OVA inoculation ($n = 6$ for each group). **(B)** Representative FACS plots of TCF1 and Tim-3 in WT and *Zbtb32*$^{-/-}$ OT-I TILs, IFNγ, and GzmB expression in WT and *Zbtb32*$^{-/-}$ T_{pex} and T_{ex} OT-I TILs. **(C)** Quantifications of the cell ratio and specific molecules of WT and *Zbtb32*$^{-/-}$ T_{pex} and T_{ex} OT-I TILs ($n = 6$ for each group). **(D)** Heatmaps showing relative expressions of different signature genes in WT and *Zbtb32*$^{-/-}$ T_{ex} OT-I TILs. **(E)** Volcanic plot showing expression levels of DEGs between WT and *Zbtb32*$^{-/-}$ T_{ex} OT-I TILs. **(F)** Lists of top GO biological pathways for DEGs that were downregulated in *Zbtb32*$^{-/-}$ T_{ex} OT-I TILs. Data are shown as means ± SEM, **P < 0.01, ***P < 0.001, and ****P < 0.0001 by paired two-tailed Student's *t* test (C). Data shown are a representative of at least two independent experiments.

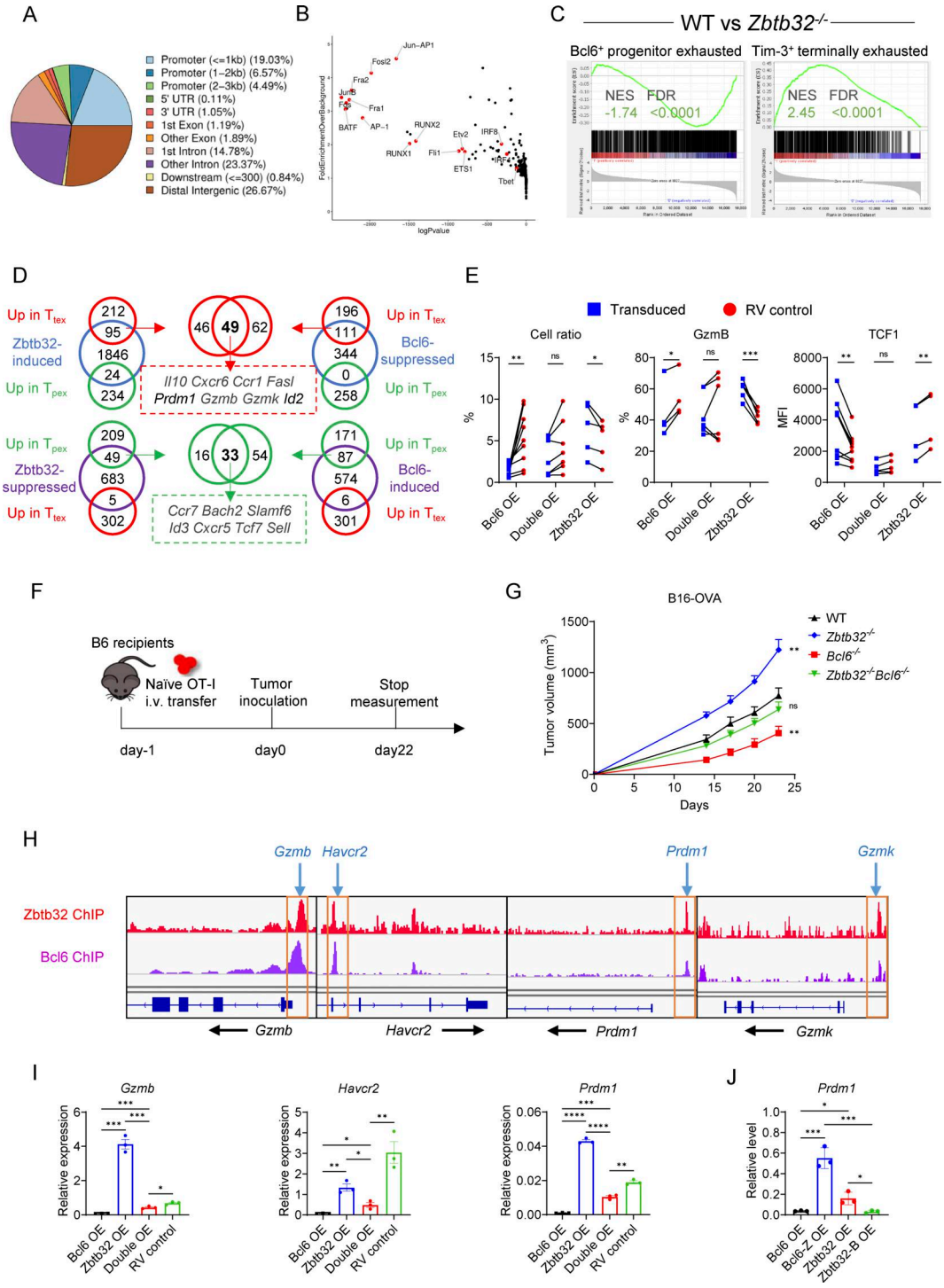

Figure S5. **Zbtb32 displays similar binding propensity but opposing regulation with Bcl6 in CD8⁺ T cells. (A)** Distribution of Zbtb32-binding peaks in CD8⁺ T cells across the genome. **(B)** Enrichment of known TF-binding motifs in binding peaks between WT and *Zbtb32*$^{-/-}$ OT-I TILs. **(C)** GSEA results for comparing the enrichment DEGs in Bcl6⁺ and Tim-3⁺ CD8⁺ T cell subsets in WT and *Zbtb32*$^{-/-}$ OT-I TILs (GEO accession: GSE114631). **(D)** Venn diagrams showing Zbtb32-regulated genes and DEGs in T_{pex} and T_{tex} CD8⁺ TILs (GEO accession: GSE114631) and Zbtb32- and Bcl6-regulated genes in CD8⁺ TILs. **(E)** Quantifications of cell ratio and specific molecules of transduced and RV control OT-I TILs, co-transferred into recipients 8 days after 1 × 10⁶ B16-OVA cell inoculation (n = 6–8 for each group). **(F)** Schematic diagram of the transfer of naïve OT-I cells. **(G)** Tumor growth in mice transplanted with 1 × 10⁶ B16-OVA cells after the transfer of 0.3 × 10⁶ naïve WT, *Zbtb32*$^{-/-}$, *Bcl6*$^{-/-}$, and *Zbtb32*$^{-/-}$*Bcl6*$^{-/-}$ OT-I cells (n = 6 for each group). **(H)** ChIP-seq data showing Zbtb32 and Bcl6 occupancy at several classic genes in CD8⁺ T cells following 4-day activation *in vitro*. **(I)** Quantifications of specific genes expressions in Bcl6-, Zbtb32-, double OE, and RV control activated CD8⁺ T cells measured by RT-qPCR (n = 3 for each group). **(J)** Expression level of *Prdm1* in Bcl6-, Bcl6-Z-, Zbtb32-, and Zbtb32-B OE activated CD8⁺ T cells measured by RT-qPCR (n = 3 for each group). GEO accessions: GSE182034, GSE182035. Data are shown as means ± SEM; ns, not significant; *P < 0.05, **P < 0.01, ***P < 0.001, and ****P < 0.0001 by paired (E) and unpaired (I and J) two-tailed Student's t test and Bonferroni-corrected two-way ANOVA (G). Data shown are a representative (G, I, and J) or a pool (E) of two independent experiments.